JNeurosci
THE JOURNAL OF NEUROSCIENCE

Research Articles: Development/Plasticity/Repair

Epac2 elevation reverses inhibition by chondroitin sulfate proteoglycans in vitro and transforms post-lesion inhibitory environment to promote axonal outgrowth in an *ex vivo* model of spinal cord injury

https://doi.org/10.1523/JNEUROSCI.0374-19.2019

Cite as: J. Neurosci 2019; 10.1523/JNEUROSCI.0374-19.2019

Received: 15 February 2019
Revised: 5 August 2019
Accepted: 8 August 2019

Epac2 elevation reverses inhibition by chondroitin sulfate proteoglycans in vitro and transforms post-lesion inhibitory environment to promote axonal outgrowth in an *ex vivo* model of spinal cord injury

Alba Guijarro-Belmar[1], Mindaugas Viskontas[1], Yuting Wei[1], Xuenong Bo[2], Derryck Shewan[1], Wenlong Huang[1],*

[1]Institute of Medical Sciences, School of Medicine, Medical Sciences & Nutrition, University of Aberdeen, Aberdeen, AB25 2ZD, United Kingdom

[2]Center for Neuroscience, Surgery and Trauma, Queen Mary University of London, London, E1 2AT, United Kingdom

Abbreviated title: Epac2 elevation promotes axonal outgrowth

***Corresponding author:** Dr Wenlong Huang, PhD, MBBS; Institute of Medical Sciences, School of Medicine, Medical Sciences & Nutrition, University of Aberdeen, Foresterhill, Aberdeen, AB25 2ZD, UK. Tel: +44 (0)461224 437290 Email: w.huang@abdn.ac.uk

Numbers: pages = 48; Figures = 11; Abstract = 249; Introduction = 650; Discussion = 1499

Conflict of Interest: The authors declare no competing financial interests.

Acknowledgements:

This work was supported by the International Spinal Research Trust, Scottish Rugby Union and RS McDonald Charitable Trust. We thank Professor Divya Chari for training with the *ex vivo* model. We also thank Dr Amer Syed, Ms Elena Moratal-Torres, Mr James W. Thomson, Ms Victoria Torsteinsbø and Dr Marieta Georgieva for their assistance with rheology and *in vitro* experiments.

Abstract

Millions of patients suffer from debilitating spinal cord injury (SCI) without effective treatments. Elevating cAMP promotes CNS neuron growth in the presence of growth-inhibiting molecules. cAMP's effects on neuron growth is partly mediated by Epac, comprising Epac1 and Epac2 – the latter predominantly expresses in postnatal neural tissue. Here, we hypothesized that Epac2 activation would enhance axonal outgrowth after SCI. Using *in vitro* assays, we demonstrated for the first time that Epac2 activation using a specific soluble agonist (S-220) significantly enhanced neurite outgrowth of postnatal rat cortical neurons and markedly overcame the inhibition by chondroitin sulphate proteoglycans and mature astrocytes on neuron growth. We further investigated the novel potential of Epac2 activation in promoting axonal outgrowth by an *ex vivo* rat model of SCI mimicking post-SCI environment *in vivo* and by delivering S-220 via a self-assembling Fmoc-based hydrogel that has suitable properties for SCI repair. We demonstrated that S-220 significantly enhanced axonal outgrowth across the lesion gaps in the organotypic spinal cord slices, compared with controls. Furthermore, we elucidated for the first time that Epac2 activation profoundly modulated the lesion environment by reducing astrocyte/microglial activation and transforming astrocytes into elongated morphology that guided outgrowing axons. Finally, we showed that S-220, when delivered by the gel at 3 weeks after contusion SCI in male adult rats, resulted in significantly better locomotor performance for up to 4 weeks post-treatment. Our data demonstrate a promising therapeutic potential of S-220 in SCI, via beneficial effects on neurons and glia post-injury to facilitate axonal outgrowth.

48 **Significance Statement**

49

50 During development, neuronal cAMP levels decrease significantly compared to the embryonic stage
51 when the nervous system is established. This has important consequences following spinal cord
52 injury (SCI), as neurons fail to regrow. Elevating cAMP levels encourages injured CNS neurons to
53 sprout and extend neurites. We have demonstrated that activating its downstream effector, Epac2,
54 enhances neurite outgrowth *in vitro,* even in the presence of an inhibitory environment. Using a
55 novel biomaterial-based drug delivery system in the form of a hydrogel to achieve local delivery of
56 an Epac2 agonist, we further demonstrated that specific activation of Epac2 enhances axonal
57 outgrowth and minimizes glial activation in an *ex vivo* model of SCI, suggesting a new strategy for
58 spinal cord repair.

59

Introduction

No cure for spinal cord injury (SCI) exists due to the complex injury nature. Obstacles to SCI repair include a lack of intrinsic growth capacity of adult mammalian CNS neurons, cavity and glial scar formation, and inhibitory molecules expressed at SCI lesions including chondroitin sulphate proteoglycans (CSPGs) and Nogo (Fawcett, 2006; Cregg et al., 2014). Multiple strategies have been developed to boost the intrinsic growth capacity of adult CNS neurons but without translational success. For example, neurotrophins enhance axonal regrowth into the lesion in rodent SCI models, but their inability to overcome inhibitory molecules makes them largely ineffective as a treatment (Hannila and Filbin, 2008). In adult mice, genetic Klf7 overexpression enhances corticospinal tract (CST) axonal regrowth into the lesion with pyramidotomy (Blackmore et al., 2012), but fails to promote regrowth beyond the lesion after SCI (Wang et al., 2017). Genetic PTEN deletion promotes axonal regrowth beyond the lesion in rodent SCI models (Danilov and Steward, 2015; Du et al., 2015; Zhou et al., 2015), but potential oncogenesis and long-term harmful effects on neurons pose concerns (Gutilla et al., 2016; Gutilla and Steward, 2016).

Elevating cAMP levels has been shown as one of the most effective ways to promote axonal regeneration and functional recovery in preclinical SCI research (Neumann et al., 2002; Qiu et al., 2002; Nikulina et al., 2004; Costa et al., 2013). Moreover, cAMP elevation overcomes inhibition on axonal outgrowth caused by myelin-associated inhibitors (Siddiq and Hannila, 2015). However, targeting cAMP is unlikely to be translated to the clinic as it is ubiquitously expressed, so its manipulation will alter functions in all types of cells. Therefore, a downstream target of cAMP more localized to neuronal cells may offer an alternative solution.

Traditionally, it was thought that cAMP solely signals through protein kinase A (PKA) to manifest its effects on axonal regeneration. However, the development of more specific tools allowed the

identification of Epac, a guanine nucleotide exchange factor for Rap1, as an intracellular target, other than PKA, directly activated by cAMP (Cheng et al., 2008). In fact, a recent study showed that the cortical infusion of a PKA antagonist, contrary to the traditional hypothesis, led to a significant increase in functional recovery in rats with SCI, suggesting the involvement of a different cAMP downstream effector in promoting axon regeneration (Wei et al., 2016).

In our previous studies, knocking-down intracellular Epac in adult rat dorsal root ganglion (DRG) neurons using siRNA led to a significant reduction in neurite outgrowth that could not be rescued by the addition of cAMP analogues (Murray and Shewan, 2008). In addition, chemo-attraction assays showed that axons are similarly attracted to a gradient of an Epac agonist as they are to a gradient of a cAMP agonist (Murray et al., 2009). Furthermore, the addition of Epac agonists to an *in vitro* SCI remyelination model significantly increased myelination and neurite outgrowth compared to controls (Boomkamp et al., 2014). Together, these studies suggest that Epac could be the key protein mediating the positive effects of cAMP on axonal growth and guidance *in vitro* (Murray and Shewan, 2008; Murray et al., 2009; Peace and Shewan, 2011b). Epac has two isoforms: Epac1 is widely expressed embryonically, while Epac2 is restricted mainly to postnatal nervous tissue (Peace and Shewan, 2011b), suggesting that targeting Epac2 could provide a neuron-specific route for manipulation to enhance axonal growth.

Therefore, our hypothesis was that the elevation of Epac2 activity by a specific agonist would enhance neurite outgrowth *in vitro* and promote axonal outgrowth in an *ex vivo* model that mimics the *in vivo* inhibitory environment after SCI. To achieve a gradual, sustained and local release of the Epac2 agonist in the injury site we explored the use of a novel self-assembling Fmoc-based hydrogel as a depot that can be directly injected into the injury site, thus representing a minimally invasive surgical procedure for future clinical translation (Zhu and Marchant, 2011; Tukmachev et al., 2016).

112 **Materials and methods**

113

114 All procedures involving the use of live animals and animal tissues were performed in accordance
115 with the UK Home Office (Scientific Procedures) Act, 1986, and were approved by the local ethics
116 committee of the University of Aberdeen.

117

118 *Cortical neuron culture.* Cortices of Sprague Dawley rats at postnatal days 0-1 (mixed sexes) were
119 harvested as a source for culturing cortical neurons. The tissue was dissociated enzymatically with
120 50 U/ml papain (Worthington, UK) in Retinal Buffer at pH 7.4 composed of 15 mM HEPES
121 (Sigma-Aldrich, UK) buffered Hanks Balanced Salts Solution (HBSS; Invitrogen, UK) containing
122 300 µM D-L cysteine (Sigma-Aldrich, UK) and incubated at 37°C for 30 min. The papain action
123 was stopped by using 10% Fetal Bovine Serum (FBS; Thermo-Fisher scientific, UK) and cells were
124 re-suspended in Neurobasal medium (Thermo-Fisher scientific, UK) supplemented with 2% B-27
125 (Thermo-Fisher scientific, UK), 1% Glutamax (Thermo-Fisher scientific, UK) and 100 U/ml
126 penicillin and 100µg/ml streptomycin (P/S; Sigma-Aldrich, UK). Cortical neurons were plated at
127 40000 neurons/ml on round 13 mm glass coverslips (BDH, UK) coated overnight with 10 µg/ml
128 poly-D-lysine (PDL; Sigma, UK) and cultured for up to 48 h at 37 °C in a 5% CO_2 / 95% air
129 incubator (NU-581DE; Nuaire, USA).

130

131 *Dorsal root ganglion (DRG) neuron and explant cultures.* DRGs were dissected from SD rats at
132 postnatal days 0-5 (mixed sexes), collected in Ham's F12 medium (Thermo-Fisher scientific, UK)
133 and trimmed to remove roots. Explants were plated directly when needed. For dissociating DRG
134 neurons, ganglia were transferred to 1 ml Retinal Buffer containing 50 U/ml papain as described
135 above. The tissue was then transferred to 100 µl HBSS containing 0.25 mg/ml trypsin inhibitor
136 (Sigma-Aldrich, UK) and 50 µg/ml DNAse (Sigma-Aldrich, UK), followed by trituration using a
137 Gilson P200 pipette until a single cell suspension was achieved. The dissociated neurons were

diluted to the required density with Neurobasal medium supplemented as described above plus nerve growth factor (NGF, 100 ng/ml; Sigma-Aldrich UK). DRG neurons were plated at 5000 neurons/ml on 13 mm coverslips coated overnight with PDL as described above and 2 µg/ml laminin (Thermo-Fisher scientific, UK) and cultured for up to 48 h at 37 °C in a 5% CO_2 / 95% air incubator.

Microglial and astrocyte cultures. Primary mixed microglia and astrocytes were cultured as previously described (Georgieva et al., 2018) from the cortices of SD rats at postnatal days 3-6 (mixed sexes) and plated on 10 µg/ml poly-D-lysine (PDL; Sigma-Aldrich, UK) coated 60 mm Petri dishes (BIOFIL Triple red TCD010060, UK). After four days of incubation at 37 °C in a 5% CO_2 / 95% air incubator, the presence of two layers of cells was confirmed: one layer of astrocytes firmly attached to the surface of the dish and a layer of microglia visible as large spherical bright cells on top of the astrocyte layer. For microglia plating, medium was collected after a gentle swirl, centrifuged at 200 ×*g* for 10 min at 4 °C and the pellet resuspended in warm medium. The microglia suspension was plated on 18 mm un-coated sterile glass coverslips and used the following day. For astrocyte plating, once microglial cells were collected, cultures were washed repeatedly with warm PBS and incubated with trypsin/EDTA 0.25% (Sigma-Aldrich, UK) for 5 min at 37 °C. Trypsin action was stopped by addition of 10% FBS, centrifuged at 200 ×g for 10 min at 4°C and re-plated in two PDL-coated flasks. Cultures were maintained for 3 weeks to ensure maturation of the astrocytes (Smith et al., 1990). Medium was changed every two days and cells were split when confluent. Microglia and astrocytes were maintained in medium composed of DMEM with 10% FBS and 100 U/ml penicillin and 100µg/ml streptomycin.

Soluble agonist and antagonist treatments for neurons in vitro. Soluble agonist Sp-8-BnT-cAMPS (S-220) and antagonist ESI-05 (both Biolog, Germany) were used according to the manufacturer's instructions for specific Epac2 activation and inactivation in neurons, respectively. In some

164 experiments, chicken extracellular chondroitin sulfate proteoglycans (CC117; Sigma-Aldrich, UK)
165 were added to culture media at 0.5 µg/ml at the time of cell plating.
166
167 *In vitro treatments for microglia and astrocytes.* Mature astrocytes were plated in 13 mm PDL-
168 coated coverslips at a density of 45,000 cells/ml. Microglia were plated in 18 mm uncoated
169 coverslip at a density of 70,000 cells/ml. Both cells types were allowed to attach and grow
170 overnight. Next morning, media were changed to serum-free media prior to treatments. Three
171 conditions were studied: control, Lipopolysaccharide (LPS) and simultaneous LPS and S-220
172 treatment. Therefore, 10 µg/ml LPS was added to the media alone or together with S-220 at 2.5 µM,
173 a concentration showing effects in promoting neurite outgrowth. The treatments were left for 4
174 hours.
175
176 *siRNA transfection.* For siRNA knockdown, DRG neurons were transfected with 3 µg of siRNA
177 duplex (Epac2 — ATC CGT GAA TGT AGT CAT TTA) (Qiagen, UK) using the Amaxa
178 Nucleofector II device (Lonza, UK) according to the manufacturer's instructions. To establish
179 transfection efficiency using this method, 3 µg of 3′-fluorescein-tagged Allstars negative control
180 siRNA (Qiagen, UK) were transfected into neonatal DRG neurons, which were plated on 2 µg/ml
181 laminin-coated glass coverslips. After 16 h cells were fixed in 4% paraformaldehyde (PFA; Sigma-
182 Aldrich, UK), immunolabeled using anti-GAP43 and analyzed using a Leica AF6000LX
183 microscope (Leica, Germany). Fluorescein-labelled neurons were compared to the total number of
184 GAP43-positive neurons to obtain the transfection efficiency, which was calculated as 80%.
185
186 *Lentiviral vector production.* We had technical limitations for the construction of lentiviral vectors
187 carrying the specific Epac2 cDNA, since the available sequence was not suitable for the subcloning
188 in the lentiviral transfer vector. Therefore, as a proof of concept we constructed Epac-LV as
189 follows. Human Epac1-YFP construct was kindly provided by Dr. Kees Jalink at The Netherlands

Cancer Institute (Amsterdam, The Netherlands). hEpac1-YFP cDNA was subcloned downstream of the CMV promoter in the lentiviral transfer vector pRRL. Self-inactivating lentiviral vectors (LV) were made by co-transfecting HEK293T cells using a three-plasmid system (Dull et al., 1998). pRRL/hEpac1-YFP or pRRL/GFP plasmids were transfected together with pPACK and pENV plasmids using the calcium precipitation method (Dull et al., 1998). Lentiviral particles were harvested 45 h after transfection and concentrated using polyethylene glycol precipitation. Viral particles were resuspended in sterile PBS after precipitation. The titers were determined by transduction of HEK293T cells using serially diluted viral stocks. The titers were 4.6 x 10^9 TU/ml for LV/hEpac1-YFP (referred as LV/Epac hereafter), and 2.2 x 10^9 TU/ml for LV/GFP. The viral stocks were aliquoted and stored at -80°C. Cortical neurons to be transduced with the LV were plated in 24 well plates (Greiner, UK) at a density of 60,000 cells/ml. 2.2 × 10^6 TU of LV/GFP or LV/hEpac1-YFP was added per well to allow transduction. Media were replaced the day after and then changed every two days. Cells were maintained for 7 days to ensure full expression of the transgenes. Anti-GFP-labelled neurons were compared to the total number of β-tubulin-(III) -positive neurons to obtain the transduction efficiency.

FRET SE microscopy. Fluorescent Resonance Energy Transfer Sensitized Emission (FRET SE) was performed in live DRG neurons as previously described (Tucker, 2014). FRET SE microscopy allowed us to demonstrate the level of Epac2 protein activity in the presence of the agonist, S-220, or the antagonist, ESI-05, respectively, in the growth cones of live DRG neurons. Two fluorophores (CFP and YFP) were fused to the two termini of Epac2 protein in the Epac FRET construct (see below). When the distance between the two is <10 nm, which occurs when the protein is inactive, a FRET signal is produced. On activation of the protein, a conformational change occurs and the distance between the two fluorophores becomes >10 nm, abolishing the FRET signal. Thus, high FRET signals correlate with low Epac2 activation and low FRET signals correlate with high Epac2 activation. Briefly, neurons were transfected with the construct mTurqDel-Epac (dDEPCD)

cp173Venus (d)-Venus (d) (H74) (Klarenbeek et al., 2011) (kindly provided by Dr. Kees Jalink, The Netherlands Cancer Institute, Amsterdam, The Netherlands) using the Amaxa Nucleofector II device. The cells were diluted in medium after transfection and cultured in 50 mm glass-bottomed dishes (MatTek, Ashland, MA) coated with PDL and 5 µg/ml laminin. One day after transfection, the medium was topped up to 5 ml and buffered with 15 mM HEPES buffer. Using a Leica AF6000LX imaging system configured correctly for FRET, images were taken of a selected growth cone in the CFP, YFP and FRET channels every 2 min for a total of 30 min. For each experiment, the first four images were taken without application to act as a baseline as the system stabilized, then the reagent was added after the fourth time point. The Epac2 agonist (S-220) was diluted to a concentration of 5 µM and the antagonist (ESI-05) to 10 µM. Analysis of each image (combining all 3 channels) was carried out using Leica Application Suite-Advanced Fluorescence software by selecting a 'region of interest' within the growth cone and recording the FRET value. These data were then expressed as a percentage change from time zero.

Choice Assay. Mature astrocytes obtained as described above were plated at 5000 cells/ml on 5 µg/ml laminin custom-made dishes. These dishes consisted of 60 mm Petri dishes (CellStar® Greiner Bio-One, UK) that had three 13 mm diameter holes in the base of the dish using a hole puncher. 18 mm coverslips were mounted onto the base of the dish using RTV 3140 coating glue (Dow corning, USA) that is non-toxic to cells. Astrocytes were left to grow for 5 h prior to plating of DRG neurons among the astrocytes. Co-cultures were further incubated at 37°C overnight in a CO_2 incubator. S-220 was added just prior to time-lapse imaging. Time-lapse recordings were taken over 30 - 60 min using NIS-element software and an okolab chamber mounted Nikon eclipse Ti inverted microscope. The response of each DRG neurite was categorized into two different categories - cross over and reflect/retract. Each response was calculated as a percentage of the total number of interactions in each experimental condition, control or S-220 treatment. Data were collated for at least 10 growth cones per condition and pooled from at least 3 separate experiments.

242

243 *Growth cone turning assays.* Assays were carried out as previously described (Murray and Shewan,
244 2008). Briefly, DRG neurons were cultured in low-walled glass-bottomed 50 mm Petri dishes
245 (MatTek, Ashland, MA) coated with 5 µg/ml laminin. The culture medium, supplemented with 15
246 mM HEPES buffer, was overlaid with a thin monolayer of warmed vegetable oil and transferred to
247 a Nikon diaphot inverted-stage microscope equipped with a stage-mounted incubator heated to
248 37°C. Growth cones were visualized using a Nikon diaphot inverted microscope connected to a PC
249 running QWin version 2.1 software (Leica, Germany). Borosilicate glass micropipettes (Intracel,
250 UK) were pulled in a Sutter pipette puller (Intracel, UK) so that they had a bore width of 1 µm.
251 Growth cones were oriented at 45° and 100 µm from a glass micropipette containing 3 - 5 µl of
252 either F12 as a control or S-220 treatment. Each reagent was ejected by an air pulse of 3 psi at 2 Hz
253 and 10 ms duration, applied to the pipette by a Picospritzer III (Intracell, UK). Each growth cone
254 was assayed for 30 min and only growth cones that had advanced at least 10 µm from the original
255 position at time zero were included. The angle between the position of the growth cone at 30 min,
256 its original position at time zero, and its original direction of growth was calculated using ImageJ
257 software. Data were collated for at least 10 growth cones per condition, pooled from at least 3
258 separate experiments.

259

260 *Hydrogel characterization.* Fmoc hydrogel is commercially available (BiogelX, UK) and can also
261 be made using published methods (Alakpa et al., 2016). Hydrogel was prepared at 2.2 mg/ml using
262 ThinCert™ cell inserts (Greiner Bio-One, UK) and following the manufacturer's instructions. RGD
263 (Arg-Gly-Asp) peptide (ab142698; Abcam, UK) at different concentrations was incorporated into
264 the gel according to the manufacturer's instructions. Rheology experiments (Discovery HR-2, TA
265 Instruments) were performed at different time-points during degradation to assess changes in gel
266 stiffness, using Frequency sweep test 0 to 100 Hz, 1% strain at 37°C. Gels were also weighed at
267 different time-points during degradation in PBS. Buffer was completely aspirated and the insert

268 weight was subtracted from the total weight. The Griess Assay was used to quantify nitrite release
269 by primary microglia when cultured with the hydrogel for 6 h. LPS (1 μg/ml; Sigma-Aldrich, UK)
270 was used as a positive activated control. Fluorescein sodium salt (Sigma-Aldrich, UK) was used to
271 assess the release profile since it has similar molecular weight compared to S-220 (MW = 376.27
272 Daltons) and can be measured by a fluorescence plate reader (Omega microplate reader; BMG
273 Labtech, UK) at 440 nm - 520 nm with 700 ms gain (Perale et al., 2012; Wilems and Sakiyama-
274 Elbert, 2015).
275
276 *Immunocytochemistry.* Cells and explants were fixed with 4% PFA in PBS for 30 min, followed by
277 incubation with 10% normal goat serum for 1 h, all at room temperature. Cells/explants were then
278 incubated with primary antibodies overnight at 4°C. We used the following primary antibodies:
279 anti-β-tubulin-(III) (1:1000, mouse; RRID: AB_1844090; Sigma-Aldrich, UK), anti-GAP43 (1:500,
280 rabbit; RRID: AB_10622060; Sigma-Aldrich, UK), anti-GFAP (1:1000, mouse; RRID: AB_94844;
281 Merk Millipore, UK), anti-Iba1 (1:1000; rabbit; RRID: AB_2314666; Wako), anti-iNOS (1:100;
282 mouse; RRID: AB_397719; BD Biosciences) and anti-GFP (1:100, chicken; RRID: AB_300798;
283 Abcam, UK). Following three washes with PBS, cells/explants were incubated for 2 h at room
284 temperature with the appropriate secondary antibodies including goat anti-mouse, rabbit or chicken
285 antibodies (1:400, RRID: AB_221544, AB_221544, AB_143160, AB_141672 and AB_141359;
286 Invitrogen). Coverslips were mounted with PBS/glycerol (1:8 ratio) after counterstaining with
287 Hoechst 33342 (2 μg/ml in PBS; Sigma-Aldrich, UK). All primary/secondary antibodies and goat
288 serum were prepared with PBS containing 0.2% Triton X-100 (Sigma-Aldrich, UK) and 0.1%
289 sodium azide (Sigma-Aldrich, UK).
290
291 *Imaging and quantification for neurite outgrowth.* A Nikon Eclipse Ti-E microscope was used to
292 acquire all images. HCA-vision (CSiRO) was used to quantify total neurite length. The plugin
293 Neuron J for ImageJ was used to manually quantify Maximal Neurite Length (MNL) of dissociated

294 neurons and maximal distance (Dmax) of neurite growth from DRG explants (Torres-Espin et al.,
295 2014). Analyses were carried out for at least 100 neurons and 10 DRG explants per condition from
296 three different experiments.
297
298 *Analysis of astrocytes and microglia activation in vitro.* For each coverslip, ten representative
299 micrographs were taken with a 20× objective. A minimum of 100 cells per condition were analysed.
300 The activation of the astrocytes was determined by the quantification of GFAP intensity
301 (Sofroniew, 2009). All images were converted into 8-bit files and the function threshold in ImageJ
302 was applied to select only area with GFAP immunoreactivity. Intensity of staining was determined
303 by the mean optical density value. The mean background fluorescence proximate to each cell was
304 subtracted from the measured fluorescence intensity of the cell area to give a corrected fluorescence
305 intensity. The activation of microglia was quantified by calculating the percentage of iNOS/Iba-1
306 double immunoreactive cells in the total Iba-1 immunoreactive cells. Data for same conditions from
307 three different replicates were averaged and compared.
308
309 *Production of spinal cord slices: ex vivo modelling of SCI.* The *ex vivo* model using rat spinal cord
310 tissue was adapted from a study using mouse spinal cord tissue (Weightman et al., 2014). The SD
311 pup's (postnatal days 0-3; mixed sexes) dorsal trunk skin surface was sprayed with 95% ethanol,
312 then a dorsal midline incision was made and skin flaps were retracted to expose the spinal column.
313 A midline incision was made along the length of the spine using fine micro-dissecting Vannas
314 spring scissors (Fine Science Tools, UK). The spinal cord was rapidly dissected from the
315 thoracolumbar region and placed in ice-cold slicing media. The meninges were gently removed and
316 a 0.7-0.9 cm length of cord was cut from the thoracic region. The cord was transferred onto an ice-
317 cold chopping plate of a pre-set McIlwain tissue chopper and sliced lengthways in the parasagittal
318 plane (350 μm thickness). Three to four slices could be derived from each cord. Slices were
319 incubated in ice for 90 min, and then selected under a dissecting microscope and transferred to pre-

cut Omnipore membrane 'confetti' (Merck Millipore, UK), resting on the Mill cell culture insert membrane (Merck Millipore, UK), using a plastic Pasteur pipette. The process of slice plating was carried out under a dissecting microscope to ensure the correct position of the slice. To avoid variability, the selected slices from each pup were plated together in one dish fitting up to four slices. Slices were cultured at the air-medium interface for up to 10 days in a humidified incubator with 5% CO_2 at 37°C with 80% medium changes every other day. The experimental unit, n, refers to slice numbers obtained from different pups.

Lesioning organotypic spinal cord slice cultures. Cords were lesioned after three days in culture. A slice lesioning tool was custom-made using a pre-assembled, double-bladed scalpel with a spacer creating a gap of approximately 700 µm. The tool was aseptically assembled prior to lesioning by taping together two surgical blades (size 15) with a spacer in the middle secured into a scalpel holder. The same lesioning tool was used in each individual experiment. The lesioning procedure was implemented inside a horizontal laminar flow hood under a dissecting microscope. To stabilize the slice in the process of lesioning the confetti was cut in a T shape allowing it to be secured with forceps while producing the lesion. A small lateral movement was used to ensure complete transection of the cord without damaging the confetti. An aspirator fitted with a pipette tip was used to remove all the debris resulting from the lesioning.

Assessment of the viability of spinal cord slices. To assess viability, three intact slices were randomly chosen before and after the lesion and incubated with the live/dead assay kit (Invitrogen, UK) containing calcein (1 µl/ml) for live cells and ethidium bromide (3 µl/ml) for dead cells, for 15 min at 37ºC. Following the incubation period slices were mounted with antifade mounting media Vectashield (Vector Laboratories, UK). Immediately afterwards, fluorescence micrographs were taken (664 µm x 834 µm) with a 10X objective with consistent exposure settings and converted to grey sale. The integrated density (mean grey value per unit area) was measured from both live- and

346 dead-stained micrographs. Thus, the viability for each slice was calculated by expressing the
347 corrected integrated density of the live-stained micrograph as a percentage of the sum total from
348 both stained groups (Cho et al., 2009). The quantification was conducted using ImageJ software.
349
350 *Treatment of spinal cord slice.* Treatment was administered immediately after the lesion either in
351 the medium or incorporated into the gels. Treatment gels were prepared 2 h before lesioning and
352 pre-cut into 700 µm x 700 µm pieces using the McIlwain tissue chopper. Gels were incorporated
353 into the injury site under the microscope using needles. Treatment was applied for 7 days.
354
355 *Immunohistochemistry.* All slices were fixed with 4% PFA 7 days after the lesion for 30 min,
356 followed by incubation with 10% normal goat serum for 1 h at room temperature. Slices were then
357 incubated with primary antibodies for 24 h at 4°C. Primary antibodies used were: anti-β (III)-
358 tubulin (1:1000, mouse;), anti-GFAP (1:500, rabbit; RRID: AB_2109645; Merk Millipore), anti-
359 GFAP (1:1000, mouse), anti-Nestin (1:400, mouse; RRID: AB_2151130; Merk Millipore), and
360 anti-Iba1 (1:1000; rabbit). Following three washes with PBS, cells were incubated for 4 h at room
361 temperature with appropriate secondary antibodies including goat anti-mouse or rabbit secondary
362 antibodies. Slices were mounted with Vectashield. All primary/secondary antibodies and goat
363 serum were prepared with PBS containing 0.2% Triton X-100 and 0.1% sodium azide.
364
365 *Image and axonal outgrowth analysis on spinal cord slices.* All fluorescence images were captured
366 with a Nikon Eclipse Ti-E microscope. Single panoramic images were generated when appropriate
367 using the Large Image tool in Nis Elements for advanced research software. Maximal Intensity
368 Projection images using multiple Z planes were also used when appropriate. Where applicable,
369 fluorescence images of immunostained slices were merged using Photoshop. Quantitative analysis
370 of β-tubulin-III stained profiles was conducted across the lesion gap from one lesion margin to the
371 other according to previously published methods (Weightman et al., 2014), with 20 division lines at

372 an equal distance of 35 µm between each line using a multi-selection plugin from ImageJ. Peak
373 analysis plugin from ImageJ was then used to convert the staining into optical density (OD) at each
374 division line covering the whole width of the lesion gap, which is equal to the width of the slice.
375 Finally, the peaks (number of staining profiles) per mm^2 per slice (Weightman et al., 2014) were
376 calculated by averaging the ODs and then divided by the area of the lesion gap.
377
378 *Analysis of astrocyte activation in spinal cord slices.* Quantitative analysis of astrocyte activation
379 was conducted by semi-quantification of GFAP staining intensity within the lesion gap. Thus, three
380 fluorescence images (478 µm x 598 µm) were taken with a 20× objective from the front areas of the
381 GFAP-immunoreactive glial scar from one half of the lesion first: the central one aligned with the
382 mid-line perpendicular to the lesion margin and then one right and one left with equal distance of
383 200 µm from the central one. We then repeated with another three fluorescence images for the other
384 half of the lesion as described above. Consistent exposures were applied for all captured images,
385 which were then converted to greyscale followed by applying a threshold using the ROI manager
386 plugin from ImageJ. Finally, the intensity of the GFAP staining from the six images per slice was
387 averaged.
388
389 Reactivity of astrocytes was also estimated by the overlapping of GFAP and Nestin as previously
390 described (O'Neill et al., 2017). Thus, three fluorescence images (478 µm x 598 µm) were taken
391 with a 20× objective from the front areas of the GFAP-Nestin immunoreactive glial scar from both
392 halves of the lesion as described above. Briefly, captured images were converted to greyscale
393 followed by the application of the "auto-threshold" function using the "Default" setting in ImageJ.
394 This generates a binary image with a black signal in a white background. "Image Calculator"
395 function in ImageJ using the "AND" operation was used to generate a third image representing the
396 regions of overlap between binary green and red. The number of overlapping pixels was calculated
397 by using the "Histogram" function in ImageJ to obtain the total number of pixels with value 255

(black). A minimum of three images was analyzed per spinal cord slice and averaged to get a final value per slice.

Analysis of microglial activation in spinal cord slices. Quantitative analysis of microglial activation was conducted by semi-quantification of the cell body perimeter of Iba-1 immunoreactive cells within the lesion gap. Thus, three fluorescence images (316 µm x 395 µm) were taken with a 30× objective as described above for astrocyte activation analysis. The perimeter (Kozlowski and Weimer, 2012) of at least 20 Iba-1 immunoreactive cells per micrograph was then measured using ImageJ and averaged for each slide. For non-lesioned microglial activation analysis, three images were taken from at least 1 mm away from the lesion site, where Iba-1-immunoreactive cells displayed non-reactive morphologies.

Treatment of contusion injured spinal cord with S-220-loaded hydrogel. For all *in vivo* experiments, young male adult Wistar rats weighing between 180 - 200 g were purchased from Envigo (Shardlow, United Kingdom). The skin and muscle overlying the spinal column were incised and a laminectomy was performed between the T9 and T10 levels. Following fixation of the adjacent T9 and T11 vertebral body to suspend the target region, a standardized moderate (12.5 mm) thoracic spinal contusion was inflicted at T10 thoracic vertebral level by the use of a NYU impactor device (MASCIS rat model III; Rutgers University, New jersey, US) as previously described (Young, 2002; Kjell and Olson, 2016). Following the injury, muscle layers were sutured and the skin was closed. Post-interventional care included manual voiding of the bladder twice a day until voiding reflex was regained. Three weeks after the induction of the injury rats were randomly allocated to treatment groups. For rats receiving treatment a 10 µl Hamilton syringe was loaded with the pre-gel format of the hydrogel using RN 26S gauge needle (26S/102/pst2/tapY) (Hamilton; Supelco, USA). The Hamilton syringe was mounted on a stereotaxic frame and armed into 45º angle. The dura was opened, and the needle was introduced into the dura with the fine controllers. A maximum of 3 µl

was injected at1 µl/min. The needle was left in place for 10 min after injection to prevent the leakage of the pre-gel solution. The dura was covered with a piece of saline-soaked gel foam, muscle layers were sutured and the skin was closed. Buprenorphine (0.3 mg/kg; Vetergesic®; Alstoe Animal Health, UK) was given s.c. for the management of acute pain after surgery and saline (0.9 % NaCl, 5 ml) was administered s.c. to compensate for any blood loss. Locomotor function was assessed by two observers independently using the 21-point Basso, Beattie & Bresnahan (BBB) open field locomotor scale on post-op days 1, 3, 14, 21, 28, 35, 42, 49.

Statistical analysis. Sigma Plot 13.0 and Origin Pro 2018b software were used for all statistical analyses. The normality test Shapiro-Wilk was performed to ensure normal distribution of the data and suitability of parametric tests. Equal variance was tested using the Brown-Forsythe test. Statistical analyses were performed using Unpaired Student's *t* test and one-way ANOVA, using Bonferroni's multiple comparison test for post-hoc analysis. If normality was not met, non-parametric tests were used: the Mann-Whitney rank sum test and the Kruskal-Wallis One-way ANOVA on ranks with Dunn's method or Tukey test post hoc correction. For *in vitro* studies, all data represent mean ± standard error of the mean (SEM).

For *ex vivo* studies, between 4 and 6 replicates were done per condition and experiment and are represented by a circle in the quantification graph. All values quoted are expressed as the mean ± SEM (box limits) ± 5% - 95% (error bars). Two-way repeated-measure ANOVA was performed for locomotor recovery (BBB scale) analysis, followed by Bonferroni's *post-hoc* multiple comparison adjustment to calculate the significant levels. "Treatment" is a between-subjects variable, while "time" is a within-subjects variable. The *in vivo* data were presented as means ± SEM. All statistical analyses were performed using Origin Pro 2018b and SigmaPlot 14.0 software. Statistical significances are indicated as $p < 0.05$ (*), $p < 0.01$ (**) and $p < 0.001$ (***).

Results

The elevation of Epac2 activity enhances neurite outgrowth in vitro

Axonal repair following SCI requires the restoration of relays from higher brain centers, such as corticospinal tracts, as well as ascending sensory pathways relaying information from the periphery to the brain. We have expertise in model systems involving cortical neurons and DRG neurons and have used both neuronal types in the current study.

Using cultured postnatal rat cortical neurons, we found that neurite outgrowth, i.e. mean total neurite length per neuron, was significantly enhanced by the treatment of S-220 at 2.5 μM for 24 h, when compared to that of the controls (agonist *vs* control: 97.5 ± 4.1 *vs* 72.8 ± 2.6 μm, p = 0.0002, unpaired Student's *t* test; Fig. 1A-C). Moreover, neurite outgrowth was significantly inhibited by bath application of ESI-05 at 10 μM for 24 h in culture (antagonist *vs* control: 50.1 ± 4.8 *vs* 77.8 ± 4.8 μm, p = 0.018, unpaired Student's *t* test; Fig. 1D-F). Furthermore, we used genetic tools such as siRNA and lentiviral vectors to illustrate the importance of Epac for neuronal growth. Thus, cortical neurons subjected to specific Epac2 siRNA knockdown for 48 h showed significantly shorter total neurite length in comparison with that of the controls (siRNA *vs* control: 131.4 ± 19.9 *vs* 183.3 ± 24.3 μm, p = 0.018, unpaired Student's *t* test; Fig. 1G-I). Similar results were also obtained for postnatal rat DRG neurons when they were treated with the S-220 (S-220 *vs* control: 991.9 ± 202.9 *vs* 399.2 ± 101.4 μm, p = 0.005787, unpaired Student's *t* test; data not shown) or when they were transfected with Epac2 siRNA (siRNA *vs* control: 889.7 ± 49.9 *vs* 1677.9 ± 105.6 μm, p= 1.1×10^{-11} unpaired Student's *t* test; data not shown). Cortical neurons were transduced with lentiviral vectors (96.7 ± 3.4 % transfection efficiency) and left to grow for 7 days to ensure protein expression. Neurons transfected with LV/Epac-YFP had significantly more neurite outgrowth when compared to that of LV/GFP transduced neurons (LV/Epac-YFP *vs* LV/GFP: 1229.2 ± 20.0 vs 795.2 ± 110.4 μm, p = 0.003, unpaired Student's *t* test; Fig. 1J-L).

Epac2 agonist activates Epac protein in DRG growth cones and attracts growth cones

To demonstrate the activation/deactivation of Epac protein by the soluble agonist S-220 and antagonist ESI-05 in neuronal growth cones, we performed FRET SE microscopy, which allowed the visualization of protein dynamics *in situ* (Tucker, 2014). DRG neurons were transfected with mTurqDel-EPAC (dDEPCD) cp173Venus (d)-Venus (d) (~40% transfection efficiency) and allowed to grow for 48 h before the experiments were performed. We found that there was a significant increase of Epac activation in growth cones during the 30 min when the S-220 was applied (S-220 *vs* baseline, $p = 8 \times 10^{-8}$, unpaired Student's *t* test; Fig. 2A-B, E). Conversely, when ESI-05 was applied, we found significantly reduced Epac activation in the growth cones when compared to the baseline (ESI-05 *vs* baseline Epac2, $p = 0.001$, unpaired Student's *t* test; Fig. 2C-D, E). Using the growth cone turning assay we examined the effect of asymmetric Epac2 activation on neonatal rat DRG neurites by creating a gradient of the S-220 agonist. Fig. 2H showed that neonatal DRG growth cones displayed a random response to a gradient of F12 culture media emitted from a micropipette placed at a 45º angle to the initial orientation of the projecting growth cones, with a mean turning angle of -1.92º ± 0.05º at 30 min. In contrast, growth cones displayed a strong chemoattraction when S-220 was emitted from the pipette (Fig. 2F-G), and the mean turning angle of 12.7º ± 4.1º at 30 min was significantly greater than that of F12 culture media ($p = 0.045$, unpaired Student's *t* test; Fig. 2H).

The elevation of Epac2 activity overcomes inhibitory effects on cortical neuron growth in vitro

To further explore the potential of Epac2 activation as a promising strategy to promote axonal outgrowth in the post-SCI environment, we cultured postnatal rat cortical neurons together with CSPGs, which significantly inhibited the outgrowth of cortical neurons by 32.1 ± 8.7% as compared to the controls ($p = 0.003$, Mann-Whitney Rank Sum test; Fig. 3A-B, D). S-220 treatment was able to overcome the inhibitory effect of CSPGs on the mean total neurite length per cortical neuron (CSPGs + S-220 *vs* CSPGs: 32.1 ± 8.7 *vs* 8.7 ± 3.3%, $p = 0.007$, Mann-Whitney Rank Sum test; Fig. 3B-D). We then analyzed the response of the growth cones of DRG neurons when they encountered inhibitory mature

502 astrocytes. This assay was performed in DRG neurons as it was optimized for this primary neural type.
503 The growth cones had the choice of either growing over astrocytes or remaining on the laminin substrate
504 during a period of 30 min time-lapse. Growth cone response behaviors were classified into two
505 categories: retract/reflect and crossover, respectively (Fig. 3 E-F). When S-220 was added to the co-
506 cultures, we found a significantly increased proportion of growth cones growing over astrocytes in
507 comparison to that of the controls (S-220 *vs* control: 45.7 ± 10.3 *vs* 11.2 ± 4.2%, p = 0.0216, unpaired
508 Student's *t* test; Fig. 3G). Conversely, we found a significant reduction in the proportion of
509 retracting/reflecting growth cones (S-220 *vs* control: 54.3 ± 10.8 *vs* 88.8 ± 8.7%, p = 0.0306, unpaired
510 Student's *t* test; Fig. 3G).
511
512 *The elevation of Epac2 activity by S-220 modulates LPS-activated astrocytes and microglia*
513 In order to assess whether S-220 has an effect in preventing and/or modulating the activation of the
514 astrocytes and microglia *in vitro*, we perform a simultaneous treatment study in which S-220 was given
515 at the same time with 10 µg/ml LPS. Previous experiments in the lab demonstrated that the treatment of
516 10 µg/ml LPS for four hours allowed rapid activation of the microglia and astrocytes cells without
517 inducing apoptosis (Georgieva, 2018).
518
519 The mean GFAP expression of astrocytes treated with LPS (Fig. 4B) was increased compared to controls
520 (Fig. 4A) (LPS *vs* control: 27.9 ± 1.8 *vs* 18.4 ± 0.9, p = $3x10^{-6}$, one-way ANOVA, Bonferroni's post
521 hoc; Fig. 4G). The simultaneous treatment of LPS and S-220 (Fig. 4C) showed a significant reduction of
522 GFAP intensity compared with LPS-treated astrocytes (LPS + S220 *vs* LPS: 20.7 ± 0.8 *vs* 27.9 ± 1.8, p =
523 $2x10^{-4}$, one-way ANOVA, Bonferroni's post hoc; Fig. 4G), being not significantly different to that of the
524 control ones (LPS + S220 *vs* control: 20.7 ± 0.8 *vs* 18.4 ± 0.9, p = 0.57, one-way ANOVA, Bonferroni's
525 post hoc; Fig. 4G). Astrocyte morphology was different within groups. LPS treated astrocytes (Fig. 4B)
526 became reactive, characterized by hypertrophic processes, broader cell bodies and tend to cluster

527 together. When astrocytes were simultaneously exposed to LPS and S-220 (Fig. 4C), they preserved
528 non-reactive morphology with slender processes similar to that of the control (Fig. 4A).
529
530 Microglia reactivity was quantified as the percentage of iNOS marker immunoreactivity. The percentage of
531 iNOS expression of microglia treated with LPS (Fig. 4E) was increased compared to controls (Fig. 4D)
532 (LPS *vs* control: 45.8 ± 2.9 *vs* 4 ± 1.3, $p = 1.5x10^{-16}$, one-way ANOVA, Bonferroni's post hoc; Fig. 4H).
533 The simultaneous treatment of LPS and S-220 (Fig. 4F) showed a significant reduction of percentage of
534 iNOS expression compared with LPS-treated microglia (LPS + S220 *vs* LPS: 24.7 ± 3.8 *vs* 45.8 ± 2.9, p
535 $= 3.4x10^{-6}$, one-way ANOVA, Bonferroni's post hoc; Fig. 4H), being also significantly different to that
536 of the control ones (LPS + S220 *vs* control: 24.7 ± 3.8 *vs* 4 ± 1.3, $p = 6.1x10^{-6}$, one-way ANOVA,
537 Bonferroni's post hoc; Fig. 4H). Moreover, the simultaneous treatment of LPS and S-220 showed a
538 significant reduction of nitrite release compared with LPS-treated microglia (LPS + S220 *vs* LPS: 0.7 ±
539 0.2 *vs* 11.8 ± 0.9, p = 0.0002, unpaired Student's *t* test; Fig. 4I).
540
541 *Fmoc-based hydrogel shows suitable properties for spinal cord repair*
542 Self-assembling Fmoc-based hydrogel was used as a delivery depot for S-220 agonist and therefore, its
543 suitability for spinal repair needed to be tested. The hydrogel (Fig. 5A) at 2.5 mM had a stiffness of
544 ~100 Pa (Fig. 5C). We found that the hydrogel degraded gradually *in vitro* in PBS at 37°C, which was
545 manifested by the reduction in gel stiffness [$(H (2) = 95.27$, $p = 2 \times 10^{-14}$, Kruskal-Wallis ANOVA on
546 Ranks with Tukey post hoc; Fig. 5C] and gel mass over time [one-way ANOVA ($F (4,25) = 50.087$,
547 $p=1.4 \times 10^{-11}$ with Bonferroni's post hoc; data not shown]. Minimal activation of gel-exposed microglia
548 was found by measuring nitrite release in culture media, contrasting to the significant nitrite release
549 observed using activating agent LPS alone (Fig. 5B). Using fluorescein, which has a similar molecular
550 weight compared to the Epac2 agonist, we estimated the cumulative release of the agonist from the
551 hydrogel (Perale et al., 2012; Wilems and Sakiyama-Elbert, 2015). The hydrogel showed a two-phase
552 release profile over a 28-day period, i.e. a quick release during the first 7 days followed by a minimal

553 gradual release over the next three weeks (Fig. 5D). The hydrogel can also incorporate functional motifs
554 such as arginine-glycine-aspartate (RGD) peptides to promote cell adhesion (Zhou et al., 2009). Here,
555 we demonstrated that the hydrogel can be functionalized with RGD peptides at different concentrations,
556 with the 1.6 mM being the optimal for neurite outgrowth (Dmax) of postnatal rat DRG explants
557 [($F(3,16)= 7.06$, $p = 0.003$; No-RGD *vs* 1.6 mM RGD: 535 ± 3 *vs* 975 ± 3 μm, $p = 0.0035$; No-RGD *vs*
558 3.2 mM RGD: 535 ± 29 *vs* 839 ± 60 μm, $p = 0.0039$; one-way ANOVA with Bonferroni's post hoc; Fig.
559 5E-H]. At this optimal concentration of RGD, we observed that the 2-D neurite outgrowth of dissociated
560 postnatal rat DRG neurons, i.e. maximal neurite length per neuron, was comparable to that seen in gels
561 without RGD (31.8 ± 5.2 *vs* 24.5 ± 3.8 μm, $p = 0.137$, unpaired Student's *t* test; data not shown).
562 However, we found significantly increased 2-D neurite outgrowth of postnatal rat cortical neurons with
563 gels functionalized with 1.6 mM RGD, when compared to that of non-functionalized gels (71.4 ± 9.2 *vs*
564 17.3 ± 4.3 μm, $p = 1.2 \times 10^{-6}$, unpaired Student's *t* test; Fig. 5I-K). Furthermore, we observed that the
565 functionalized hydrogel supported excellent 3-D neurite growth of DRG explants and DRG neurons
566 (Fig. 5L-N). For simplicity, we refer to the hydrogel functionalized with 1.6 mM RGD hereafter as "the
567 hydrogel".
568
569 *The elevation of Epac2 activity enhances 2-D neurite outgrowth with Fmoc hydrogel in vitro*
570 As a proof-of-concept, we first explored combination of the Epac2 activation strategy with the gel by
571 adding the S-220 agonist in the media of cultures where DRG explants or DRG neurons grew on the gel
572 surface. We demonstrated that there was a significant increase in neurite outgrowth of DRG explants
573 growing on the gel and simultaneously treated with the agonist when compared to that with the gel alone
574 [S-220 + gel *vs* gel only: 1141.4 ± 159.9 *vs* 608.3 ± 93.9 μm (Dmax), $p = 0.029$, unpaired Student's *t*
575 test; Fig. 6A-C]. In addition, we found that the neurite outgrowth of dissociated DRG neurons was
576 significantly enhanced by combining S-220 and the gel in comparison to that of the gel alone [S-220 +
577 gel *vs* gel only: 57.3 ± 6.5 *vs* 31.9 ± 5.3 μm (mean total neurite length per neuron), $p = 0.002$, unpaired
578 Student's *t* test; Fig. 6D-F].

The elevation of Epac2 activity promotes axonal outgrowth in an ex vivo model of SCI

To further demonstrate the potential of Epac2 activation for spinal cord repair, we adapted a previously established mouse *ex vivo* model of SCI using postnatal rat spinal cord organotypic slices (Weightman et al., 2014). The study design, timeline and schematic diagram of the methodology are shown in Fig. 7A-B. First, we used a live/dead assay to measure the viability of the slices. The results showed that there was no difference in the percentage of cells labelled by the cell death marker before and after lesioning the slices (8.4 ± 3.1 *vs* 4.6 ± 2.1%, p = 0.148, unpaired Student's *t* test; Fig. 7C-D). We then treated the lesioned slices with S-220 being applied to the culture medium alone, or S-220 applied to the culture medium together with hydrogels (not containing S-220) being placed into lesion gaps (Fig. 7E-I). One-way ANOVA showed that there was a significant treatment effect on axonal outgrowth across the lesion gap among different treatment groups [$F(3,19) = 8.547$, $p=0.0006$; Fig. 7G]. Thus, the results showed that the number of β-tubulin-III staining profiles per mm^2 per slice was significantly higher in the slices treated with the agonist and the gel when compared to those of the control, gel alone, and S-220 alone groups [S-220 + gel *vs* control, S-220 alone, and gel alone: 3016.5 ± 596.5 *vs* 821.8 ± 102.9 ($p = 0.00055$), 1247.9 ± 73.7 ($p = 0.005$), and 1694.7 ± 82.9 ($p = 0.0481$), one-way ANOVA with Bonferroni's post hoc; Fig. 7G].

Epac2 agonist incorporated into Fmoc hydrogel promotes axonal outgrowth

Our next step was to incorporate S-220 into the gel so that the agonist could be locally released and delivered to the injury site. Since it is a different delivery method, we tested different concentrations of the agonist in order to identify the optimal concentration. One-way ANOVA showed that there was a significant concentration effect on axonal outgrowth across the lesion gap [$F(2,12) = 21.53$, $p = 0.00011$; Fig. 8D]. Thus, the results showed that the number of β-tubulin-III staining profiles per mm^2 per slice

was significantly higher in the slices treated with the gel+S-220 (5 μM) in comparison to those of the gel+S-220 (2.5 μM) and gel+S-220 (10 μM) [gel+S-220 (5 μM) *vs* gel+ S-220 (2.5 μM) or gel+ S-220 (10 μM): 3613.0 ± 177.0 *vs* 1457.6 ± 284.6 ($p = 0.000091$) or 2289.8 ± 298.2 ($p = 0.0086$), one-way ANOVA with Bonferroni's post hoc test; Fig. 8A-D]. Once the optimal concentration of the agonist was established, we then investigated the efficacy of the agonist at this concentration when it was incorporated into the gel in promoting neurite outgrowth across the lesion gap. One-way ANOVA showed that there was a significant treatment effect on axonal outgrowth among different experimental groups [$F(4,22) = 21.14$, $p = 7 \times 10^{-8}$; Fig. 8A-D]. Thus, the results showed that the number of β-tubulin-III staining profiles per mm^2 per slice was significantly higher in the slices treated with the gel+ S-220 (5 μM) when compared to those of the control and gel only groups [gel+ S-220 (5 μM) *vs* control or gel only: 3613 ± 177 *vs* 743 ± 81.5 ($p = 3 \times 10^{-8}$) or 1698.5 ± 169.4 ($p=0.000003$), Bonferroni's post hoc; Fig. 8A-D].

The elevation of Epac2 activity attenuates the activation of astrocytes in an ex vivo model of SCI

GFAP staining intensity within the lesion gap was quantified to assess astrocyte reactivity. A marked difference was found in the morphology of the astrocytes across the lesion gap from different experimental groups. GFAP immunoreactive cells at the forefront into the lesion gap in slices without any treatments were intensively labelled and hypertrophic (Fig. 8E). Slices treated with the gel only presented a mixed pattern of GFAP immunoreactive cells (Fig. 8F), while those slices receiving S-220 treatment delivered by the gel presented GFAP immunoreactive cells that were lightly labelled and had elongated polygonal morphologies (Fig. 8G). One-way ANOVA showed that there was a significant treatment effect on GFAP activation across the lesion gap among different experimental groups [$F(2,15) = 76.79$, $p = 1 \times 10^{-7}$; Fig. 8H]. Thus, the results showed that GFAP intensity in the slices treated with the agonist and the gel was significantly lower than those of the control or gel alone groups [gel+ S-220 *vs* control or gel only: 18.2 ± 1.1 *vs* 33.5 ± 0.5 ($p = 8 \times 10^{-8}$) or 25.7 ± 0.9 ($p = 0.00004$), one-way ANOVA Bonferroni's post hoc test; Fig. 8H]. We then performed double staining for β-tubulin-III and GFAP to

study the relationship between astrocytes (hypertrophic and non-hypertrophic) and regrown neurites. In non-treated slices highly reactive astrocytes appeared to act as a barrier for neurite outgrowth (Fig. 8I). Higher magnification images demonstrated collapsed growth cones when they confronted highly reactive astrocytes (Fig. 8J). Conversely, in the slices receiving S-220 delivered by the gel we observed a close relationship between β-tubulin-III stained neurite profiles and GFAP stained astrocyte processes (Fig. 8K). Higher magnification images demonstrated that regrown axons were indeed aligned to astrocyte processes (Fig. 8M).

Overlapping of nestin and GFAP markers was also quantified as a reactivity parameter as previously described (O'Neill et al., 2017). One-way ANOVA showed that there was a significant treatment effect on nestin/GFAP overlapping across the lesion gap among different experimental groups [$F(2, 16) = 11.6$, $p = 0.0001$; Fig. 8P]. Thus, the results showed that the mean nestin/GFAP overlapping pixels were significantly lower in the slices treated with S-220 delivered by the gel, when compared to those of the control or gel alone groups [gel + S-220 *vs* control or gel only: 48369.4 ± 16194.2 *vs* 140811.6 ± 12992.8 ($p = 0.003$) or 141925.5 ± 19180.4 ($p = 0.002$), Bonferroni's post hoc; Fig. 8N-P].

The elevation of Epac2 activity attenuates microglial activation in an ex vivo model of SCI

We used the Iba-1 marker to identify microglia in lesioned slices. We found that, within the lesion site, Iba-1 immunoreactive cells displayed a highly activated morphology (large in cell size and with no processes) in those slices without any treatments (Fig. 9A, white asterisks). This activated morphology was in contrast to those Iba-1 immunoreactive cells located in the main body of the slices away from the lesion margins (Fig. 9C, yellow arrowheads) that exhibited a non-activated morphology (small in cell size and with ramified processes). However, we observed that in those slices treated with S-220 delivered by the gel, Iba-1 immunoreactive cells within the lesion site resembled the non-activated morphology seen in the main slice body (Fig. 9B, yellow arrowheads). We then performed a quantification to determine the differences in Iba-1 immunoreactive cells within the lesion site among

different experimental groups by measuring cell body perimeter, which has been shown to correlate with microglial activation (Kozlowski and Weimer, 2012). Thus, the results showed that the mean cell body perimeter of Iba-1 immunoreactive cells per slice was significantly smaller in the slices treated with S-220 and the gel in comparison to those of the control or gel alone groups [gel + S-220 *vs* control or gel alone: 93 ± 4.2 *vs* 123.7 ± 1.7 µm ($p = 0.000091$) or 103.1 ± 2.3 µm ($p = 0.0086$), Bonferroni's post hoc test; Fig. 9D]. In those slices receiving S-220 delivered by the gel we found that the mean cell body perimeter of Iba-1 immunoreactive cells was similar to that of non-activated microglia seen in the main slice body (gel + S-220 *vs* non-activated microglia in the main slice body: 93 ± 4.2 *vs* 81.7 ± 2.4 µm, $p = 0.115$, unpaired Student's *t* test; Fig. 9D]. The relationship between GFAP immunoreactive and Iba-1 immunoreactive cells was investigated by examining the co-labeling of these two markers. In non-treated slices, we observed that highly reactive astrocytes were intermingled with large, amoeboid and congregated Iba-1 immunoreactive cells (Fig. 9E), demonstrating that both activated glial cells formed a highly inhibitory environment for neurite outgrowth. In contrast, in the slices receiving S-220 delivered by the gel we observed smaller non-activated Iba-1 immunoreactive cells, which were sparsely spread around elongated polygonal GFAP immunoreactive cells (Fig. 9F).

S-220 delivered by Fmoc hydrogel promotes functional recovery after a spinal cord contusion injury

Injured rats treated with S-220 delivered by the gel at three weeks post-surgery showed significant improvement in the BBB score, already detectable three weeks after treatment compared to injury-only controls, indicating better controlled limb movements after treatment with S-220-loaded gels (Fig. 10). The improvements were sustained for the rest of the study. Two-way ANOVA showed that there was significant treatment effects [$F(1,35) = 16.17$, $p < 0.001$; Fig. 10]. At week four post-treatment, contused rats that received S-220-loaded gel significantly increased locomotor behavior reaching an average BBB score of 17.3 ± 0.9, compared to 14.3 ± 1.1 for injury-only controls ($p = 0.042$, Bonferroni's *post hoc* analysis; Fig. 10).

Discussion

Promoting injured adult CNS mammalian neurons to regrow after injury remains a significant challenge in modern medicine. Among different strategies, cAMP and its downstream effectors have been shown to enhance neurons' outgrowth capacity. Here, we demonstrate for the first time, using pharmacological and genetic tools, that specific elevation of Epac2 activity, a downstream target of cAMP, significantly enhances neurite outgrowth of cultured postnatal DRG and cortical neurons. Moreover, Epac2 activation promotes significant axonal outgrowth in lesioned spinal cord slices in an *ex vivo* model of SCI. We reveal novel evidence that Epac2 elevation overcomes inhibition on neuron/axon growth by CSPGs and mature astrocytes *in vitro* and by the post-lesion environment of the *ex vivo* model.

Previously PKA was thought to be solely responsible for cAMP's effects on axonal growth (Siddiq and Hannila, 2015). However, strong evidence suggests that it is Epac, not PKA, that mediates the positive effects of cAMP in promoting axonal growth (Murray et al., 2009; Boomkamp et al., 2014; Wei et al., 2016). Several general agonists were developed to activate Epac, but not PKA, allowing the study of Epac's roles in mediating specific cAMP functions in cell signaling pathways (Enserink et al., 2002). Studies using these agonists demonstrate that Epac mediates cAMP-dependent axonal growth in: (1) embryonic, neonatal and adult rat DRG neurons (Murray and Shewan, 2008; Murray et al., 2009; Wei et al., 2016), (2) PC12 cells (Christensen et al., 2003); and (3) an *in vitro* model of SCI and remyelination (Boomkamp et al., 2014). These agonists also regulate axonal elongation in rat embryonic hippocampal neurons (Munoz-Llancao et al., 2015), and switch the proliferative signal of cAMP to a neuronal differentiation program in PC12 cells (Kiermayer et al., 2005). However, they failed to discriminate the effects between Epac1 and Epac2.

We previously showed that siRNA knockdown of Epac1 and Epac2 in adult DRG neurons significantly reduced neurite outgrowth (Murray and Shewan, 2008). However, since adult neurons

710 mainly express Epac2, our previous evidence on neurite growth is likely to be mediated solely by
711 Epac2. Here, we used an Epac2 specific agonist (S-220), which has been shown to selectively
712 activate Epac2 (Schwede et al., 2015). We are the first group to report the use of this agonist in
713 primary postnatal rat neurons and spinal cord tissue. Indeed, we used FRET to demonstrate that S-
714 220 enhanced Epac2 protein activity in the growth cones of DRG neurons. Furthermore, we
715 provided direct evidence that DRG neurons turned towards a gradient of S-220, such that Epac2
716 activation was biased towards the direction of turning. These data convincingly suggest the
717 specificity of this agonist in postnatal neurons. We and others have previously reviewed potential
718 mechanisms of Epac2 signaling in neurite outgrowth (Peace and Shewan, 2011a; Batty et al., 2017).
719 Thus, Epac2 is known to activate Rap1, which can subsequently modulate AKT (Mei et al., 2002;
720 Nijholt et al., 2008) and B-Raf-MER-ERK (Qiu et al., 2000; Enserink et al., 2002; Wang et al.,
721 2006) signaling pathways, both being shown to play essential roles in axonal growth and guidance
722 (Liu and Snider, 2001). Epac2 activation may also lead to CREB activation that has been shown to
723 promote neuroplasticity (Wei et al., 2016) (Fig. 11).
724
725 Following SCI, there are numerous molecules present at the lesion site, including CSPGs, MAG,
726 Nogo, and OMgp that are inhibitory to axonal outgrowth (Hannila and Filbin, 2008). A body of
727 evidence has shown that elevation of neuronal cAMP level overcomes the inhibition by MAG and
728 CNS myelin on axonal outgrowth (Siddiq and Hannila, 2015). The ability of cAMP elevation to
729 overcome inhibition may involve the activation of CREB, which then leads to transcriptional
730 changes in arginase I, interleukin-6, secretory leukocyte protease inhibitor, and metallothionein
731 (Hannila and Filbin, 2008; Siddiq and Hannila, 2015). Up-regulation of these genes has been shown
732 to promote axonal outgrowth (Cafferty et al., 2004; Deng et al., 2009; Ghasemlou et al., 2010;
733 Siddiq and Hannila, 2015). Here, we report that activation of Epac2 overcomes inhibition by
734 CSPGs and mature astrocytes on neuronal growth, and this could therefore be mediated through
735 CREB activation. It is important to note that Rap1 can regulate integrins, which are essential for cell

736 adhesion (Bos et al., 2003). Different cell types have been shown to control adhesion to laminin via
737 cAMP-mediated integrin regulation (Murphy et al., 2005). Therefore, Epac2 activation could
738 possibly also lead to Rap1-mediated redistribution and conformational activation of integrins in the
739 growth cone (Bos et al., 2003), thereby modifying their responses to inhibitory molecules in the
740 extracellular matrix after injury (Condic et al., 1999; Tan et al., 2011; Cheah and Andrews, 2018).
741
742 Apart from the effects on axonal outgrowth in the *ex vivo* model, we also report a significantly
743 modified lesion environment consisting of astrocytes and microglia by the Epac2 agonist.
744 Astrocytes form the major cell type that contribute to the formation of the glial scar after SCI and
745 strong evidence suggests that there is heterogeneity within astrocyte populations in the scar with
746 some cells producing axon-growth supporting molecules (Anderson et al., 2016). The morphology
747 of Epac2 agonist-treated astrocytes in our study remarkably resembles those newly proliferated and
748 elongated astrocytes at the lesion border after SCI, which are regulated by the STAT-3 signaling
749 pathway (Wanner et al., 2013) and show similarity with radial glial progenitors providing guidance
750 for neuron growth during CNS development (Garcia et al., 2004). Although the functions of these
751 elongated astrocytes at the lesion border are largely unclear, evidence suggests that they regulate
752 inflammatory cell behavior (Wanner et al., 2013). Here, we demonstrate a similar pattern following
753 S-220 treatment, in that elongated astrocytes exist among Iba-1^{+} microglia with non-activated
754 morphology at the lesion site. It is known that cAMP elevation can cause autocrine interleukin-6
755 up-regulation in astrocytes, which in turn can lead to STAT3 phosphorylation (Takanaga et al.,
756 2004). Moreover, cAMP elevation in astrocytes causes morphological change into a process-
757 bearing shape, downregulation of the genes responsible for proteoglycan production, and up-
758 regulation of the gene for the NMDA receptor subunit NR2C that is a major component of the
759 tripartite synapse regulating astrocyte-neuron communication (Paco et al., 2016). Therefore, it is
760 conceivable that in our study the S-220 has caused profound changes in astrocytes at the lesion site
761 similar to those described after cAMP elevation and render them supportive for the regrowing axons

762 (Fig. 11). Furthermore, there is evidence that cAMP elevation by a general agonist causes
763 microglial BV-2 cells to increase arginase I production and change to bipolar morphology when co-
764 treated with TNF-α (Ghosh et al., 2016). Epac activation by a general agonist also causes BV-2
765 cells to reduce their pro-inflammatory activities (Steininger et al., 2011). Hence, we propose that in
766 our study the S-220 also attenuates the activation of microglia at the lesion site. Taken together, our
767 data suggest that Epac2 elevation in both astrocytes and microglia may have potently modified the
768 lesion environment from inhibitory to permissive for axonal outgrowth.
769
770 With the novel Fmoc-based hydrogel used as a delivery depot for sustained release of S-220, our
771 study confers translational potential. We demonstrate for the first time that this hydrogel has
772 excellent biocompatibility and supports excellent neurite outgrowth *in vitro* and axonal outgrowth
773 in the *ex vivo* model. Moreover, its stiffness can be tuned to be similar to CNS tissue properties,
774 which is a key requirement for spinal cord repair (Georges et al., 2006). Furthermore, the hydrogel
775 can be developed as injectable formats that can fully plug lesion cavities, thus representing a
776 minimally invasive neurosurgical technique (Cigognini et al., 2011; Kabu et al., 2015). In an
777 exploratory pilot study, we injected the S-220 loaded Fmoc hydrogel into the lesion cavity of rats
778 with contusion SCI at a subacute stage i.e. 3 weeks post-injury and found significantly improved
779 locomotor functional recovery when compared with animals with contusion only. However, further
780 *in vivo* immunohistochemical and functional studies are required to validate the potential of these
781 treatments in SCI, which is beyond the scope of the current study. Future studies also need to
782 further optimize the injected hydrogel volume and S-220 dose and establish the *in vivo* effects of S-
783 220 on axonal outgrowth and glial activation.
784
785 The failure to find a cure for spinal cord repair is mainly due to the complex injury nature of SCI.
786 Many studies have designed strategies, either alone or in combination, to tackle various obstacles
787 presented by the injury, but so far have failed to translate results to the clinic. Our findings using

Epac2 elevation to promote spinal cord repair underpin a significant game change not only in directly enhancing the intrinsic capacity of injured neurons to regrow, but moreover in harnessing the inhibitory environment, including the glial scar and microglia, to facilitate axonal outgrowth. However, caution is needed when extrapolating our strategy to other CNS injuries such as brain injury and stroke, as recent preclinical evidence suggests that, in the acute phase of hemorrhage-induced brain trauma, increased neuronal expression of Epac2 leads to apoptosis (Zhuang et al., 2019). Future studies are required to fully understand the role of Epac2 under different CNS injury pathogeneses.

References

Alakpa EV, Jayawarna V, Lampel A, Burgess KV, West CC, Bakker SCJ, Roy S, Javid N, Fleming S, Lamprou DA, Yang JL, Miller A, Urquhart AJ, Frederix PWJM, Hunt NT, Peault B, Ulijn RV, Dalby MJ (2016) Tunable Supramolecular Hydrogels for Selection of Lineage-Guiding Metabolites in Stem Cell Cultures (vol 1, pg 298, 2016). Chem-Us 1:512-512.

Anderson MA, Burda JE, Ren Y, Ao Y, O'Shea TM, Kawaguchi R, Coppola G, Khakh BS, Deming TJ, Sofroniew MV (2016) Astrocyte scar formation aids central nervous system axon regeneration. Nature 532:195-200.

Batty NJ, Fenrich KK, Fouad K (2017) The role of cAMP and its downstream targets in neurite growth in the adult nervous system. Neuroscience letters 652:56-63.

Blackmore MG, Wang Z, Lerch JK, Motti D, Zhang YP, Shields CB, Lee JK, Goldberg JL, Lemmon VP, Bixby JL (2012) Kruppel-like Factor 7 engineered for transcriptional activation promotes axon regeneration in the adult corticospinal tract. Proceedings of the National Academy of Sciences of the United States of America 109:7517-7522.

Boomkamp SD, McGrath MA, Houslay MD, Barnett SC (2014) Epac and the high affinity rolipram binding conformer of PDE4 modulate neurite outgrowth and myelination using an in vitro spinal cord injury model. British journal of pharmacology 171:2385-2398.

Bos JL, de Bruyn K, Enserink J, Kuiperij B, Rangarajan S, Rehmann H, Riedl J, de Rooij J, van Mansfeld F, Zwartkruis F (2003) The role of Rap1 in integrin-mediated cell adhesion. Biochem Soc Trans 31:83-86.

Cafferty WB, Gardiner NJ, Das P, Qiu J, McMahon SB, Thompson SW (2004) Conditioning injury-induced spinal axon regeneration fails in interleukin-6 knock-out mice. J Neurosci 24:4432-4443.

Cheah M, Andrews MR (2018) Integrin Activation: Implications for Axon Regeneration. In: Cells.

822 Cheng X, Ji Z, Tsalkova T, Mei F (2008) Epac and PKA: a tale of two intracellular cAMP receptors.
823 Acta biochimica et biophysica Sinica 40:651-662.

824 Cho JS, Park HW, Park SK, Roh S, Kang SK, Paik KS, Chang MS (2009) Transplantation of
825 mesenchymal stem cells enhances axonal outgrowth and cell survival in an organotypic spinal
826 cord slice culture. Neuroscience letters 454:43-48.

827 Christensen AE, Selheim F, de Rooij J, Dremier S, Schwede F, Dao KK, Martinez A, Maenhaut C,
828 Bos JL, Genieser HG, Doskeland SO (2003) cAMP analog mapping of Epac1 and cAMP kinase.
829 Discriminating analogs demonstrate that Epac and cAMP kinase act synergistically to promote
830 PC-12 cell neurite extension. The Journal of biological chemistry 278:35394-35402.

831 Cigognini D, Satta A, Colleoni B, Silva D, Donega M, Antonini S, Gelain F (2011) Evaluation of
832 early and late effects into the acute spinal cord injury of an injectable functionalized self-
833 assembling scaffold. PLoS One 6:e19782.

834 Condic ML, Snow DM, Letourneau PC (1999) Embryonic neurons adapt to the inhibitory
835 proteoglycan aggrecan by increasing integrin expression. The Journal of neuroscience : the
836 official journal of the Society for Neuroscience 19:10036-10043.

837 Costa LM, Pereira JE, Filipe VM, Magalhaes LG, Couto PA, Gonzalo-Orden JM, Raimondo S, Geuna
838 S, Mauricio AC, Nikulina E, Filbin MT, Varejao AS (2013) Rolipram promotes functional
839 recovery after contusive thoracic spinal cord injury in rats. Behavioural brain research 243:66-73.

840 Cregg JM, DePaul MA, Filous AR, Lang BT, Tran A, Silver J (2014) Functional regeneration beyond
841 the glial scar. Experimental neurology 253:197-207.

842 Danilov CA, Steward O (2015) Conditional genetic deletion of PTEN after a spinal cord injury
843 enhances regenerative growth of CST axons and motor function recovery in mice. Experimental
844 neurology 266:147-160.

845 Deng J, Zhang XL, Wang JW, Teng LL, Ge J, Takemori H, Xiong ZQ, Zhou Y (2009) Expression
846 and regulated nuclear transport of transducers of regulated CREB 1 in retinal ganglion cells.
847 Neuroscience 159:1023-1031.

848 Du K, Zheng S, Zhang Q, Li S, Gao X, Wang J, Jiang L, Liu K (2015) Pten Deletion Promotes
849 Regrowth of Corticospinal Tract Axons 1 Year after Spinal Cord Injury. The Journal of
850 neuroscience : the official journal of the Society for Neuroscience 35:9754-9763.

851 Dull T, Zufferey R, Kelly M, Mandel RJ, Nguyen M, Trono D, Naldini L (1998) A third-generation
852 lentivirus vector with a conditional packaging system. J Virol 72:8463-8471.

853 Enserink JM, Christensen AE, de Rooij J, van Triest M, Schwede F, Genieser HG, Doskeland SO,
854 Blank JL, Bos JL (2002) A novel Epac-specific cAMP analogue demonstrates independent
855 regulation of Rap1 and ERK. Nat Cell Biol 4:901-906.

856 Fawcett JW (2006) Overcoming inhibition in the damaged spinal cord. Journal of neurotrauma
857 23:371-383.

858 Garcia AD, Doan NB, Imura T, Bush TG, Sofroniew MV (2004) GFAP-expressing progenitors are
859 the principal source of constitutive neurogenesis in adult mouse forebrain. Nat Neurosci 7:1233-
860 1241.

861 Georges PC, Miller WJ, Meaney DF, Sawyer ES, Janmey PA (2006) Matrices with compliance
862 comparable to that of brain tissue select neuronal over glial growth in mixed cortical cultures.
863 Biophys J 90:3012-3018.

864 Georgieva M (2018) The potential of omega-3 polyunsaturated fatty acids in he prevention and
865 treatment of central neuropathic pain after spinal cord injury. In: The School of Medicine,
866 Medical Sciences and Nutrition: University of Aberdeen

867 Georgieva M, Leeson-Payne A, Dumitrascuta M, Rajnicek A, Malcangio M, Huang W (2018) A
868 refined rat primary neonatal microglial culture method that reduces time, cost and animal use. J
869 Neurosci Methods 304:92-102.

870 Ghasemlou N, Bouhy D, Yang J, Lopez-Vales R, Haber M, Thuraisingam T, He G, Radzioch D, Ding
871 A, David S (2010) Beneficial effects of secretory leukocyte protease inhibitor after spinal cord
872 injury. Brain 133:126-138.

873 Ghosh M, Xu Y, Pearse DD (2016) Cyclic AMP is a key regulator of M1 to M2a phenotypic
874 conversion of microglia in the presence of Th2 cytokines. J Neuroinflammation 13:9.

875 Gutilla EA, Steward O (2016) Selective neuronal PTEN deletion: can we take the brakes off of
876 growth without losing control? Neural regeneration research 11:1201-1203.

877 Gutilla EA, Buyukozturk MM, Steward O (2016) Long-term consequences of conditional genetic
878 deletion of PTEN in the sensorimotor cortex of neonatal mice. Experimental neurology 279:27-
879 39.

880 Hannila SS, Filbin MT (2008) The role of cyclic AMP signaling in promoting axonal regeneration
881 after spinal cord injury. Experimental neurology 209:321-332.

882 Kabu S, Gao Y, Kwon BK, Labhasetwar V (2015) Drug delivery, cell-based therapies, and tissue
883 engineering approaches for spinal cord injury. Journal of controlled release : official journal of
884 the Controlled Release Society 219:141-154.

885 Kiermayer S, Biondi RM, Imig J, Plotz G, Haupenthal J, Zeuzem S, Piiper A (2005) Epac activation
886 converts cAMP from a proliferative into a differentiation signal in PC12 cells. Mol Biol Cell
887 16:5639-5648.

888 Kjell J, Olson L (2016) Rat models of spinal cord injury: from pathology to potential therapies.
889 Disease models & mechanisms 9:1125-1137.

890 Klarenbeek JB, Goedhart J, Hink MA, Gadella TWJ, Jalink K (2011) A mTurquoise-based cAMP
891 sensor for both FLIM and ratiometric read-out has improved dynamic range. PloS one 6:e19170.

892 Kozlowski C, Weimer RM (2012) An automated method to quantify microglia morphology and
893 application to monitor activation state longitudinally in vivo. PloS one 7:e31814.

894 Liu RY, Snider WD (2001) Different signaling pathways mediate regenerative versus developmental
895 sensory axon growth. Journal of Neuroscience 21.

896 Mei FC, Qiao JB, Tsygankova OM, Meinkoth JL, Quilliam LA, Cheng XD (2002) Differential
897 signaling of cyclic AMP - Opposing effects of exchange protein directly activated by cyclic AMP
898 and cAMP-dependent protein kinase on protein kinase B activation. Journal of Biological
899 Chemistry 277:11497-11504.

900 Munoz-Llancao P, Henriquez DR, Wilson C, Bodaleo F, Boddeke EW, Lezoualc'h F, Schmidt M,
901 Gonzalez-Billault C (2015) Exchange Protein Directly Activated by cAMP (EPAC) Regulates
902 Neuronal Polarization through Rap1B. The Journal of neuroscience : the official journal of the
903 Society for Neuroscience 35:11315-11329.

904 Murphy MM, Zayed MA, Evans A, Parker CE, Ataga KI, Telen MJ, Parise LV (2005) Role of Rap1
905 in promoting sickle red blood cell adhesion to laminin via BCAM/LU. Blood 105:3322-3329.

906 Murray AJ, Shewan DA (2008) Epac mediates cyclic AMP-dependent axon growth, guidance and
907 regeneration. Molecular and cellular neurosciences 38:578-588.

908 Murray AJ, Tucker SJ, Shewan DA (2009) cAMP-dependent axon guidance is distinctly regulated by
909 Epac and protein kinase A. The Journal of neuroscience : the official journal of the Society for
910 Neuroscience 29:15434-15444.

911 Neumann S, Bradke F, Tessier-Lavigne M, Basbaum AI (2002) Regeneration of sensory axons within
912 the injured spinal cord induced by intraganglionic cAMP elevation. Neuron 34:885-893.

913 Nijholt IM, Dolga AM, Ostroveanu A, Luiten PGM, Schmidt M, Eisel ULM (2008) Neuronal
914 AKAP150 coordinates PKA and Epac-mediated PKB/Akt phosphorylation. Cell Signal 20:1715-
915 1724.

916 Nikulina E, Tidwell JL, Dai HN, Bregman BS, Filbin MT (2004) The phosphodiesterase inhibitor
917 rolipram delivered after a spinal cord lesion promotes axonal regeneration and functional
918 recovery. Proceedings of the National Academy of Sciences of the United States of America
919 101:8786-8790.

920 O'Neill P, Lindsay SL, Pantiru A, Guimond SE, Fagoe N, Verhaagen J, Turnbull JE, Riddell JS,
921 Barnett SC (2017) Sulfatase-mediated manipulation of the astrocyte-Schwann cell interface. Glia
922 65:19-33.

923 Paco S, Hummel M, Pla V, Sumoy L, Aguado F (2016) Cyclic AMP signaling restricts activation and
924 promotes maturation and antioxidant defenses in astrocytes. BMC Genomics 17:304.

925 Peace AG, Shewan DA (2011a) New perspectives in cyclic AMP-mediated axon growth and
926 guidance: The emerging epoch of Epac. Brain research bulletin 84:280-288.

927 Peace AG, Shewan DA (2011b) New perspectives in cyclic AMP-mediated axon growth and
928 guidance: The emerging epoch of Epac. Brain research bulletin 84:280-288.

929 Perale G, Rossi F, Santoro M, Peviani M, Papa S, Llupi D, Torriani P, Micotti E, Previdi S, Cervo L,
930 Sundstrom E, Boccaccini AR, Masi M, Forloni G, Veglianese P (2012) Multiple drug delivery
931 hydrogel system for spinal cord injury repair strategies. Journal of controlled release : official
932 journal of the Controlled Release Society 159:271-280.

933 Qiu J, Cai D, Dai H, McAtee M, Hoffman PN, Bregman BS, Filbin MT (2002) Spinal axon
934 regeneration induced by elevation of cyclic AMP. Neuron 34:895-903.

935 Qiu WS, Zhuang SH, von Lintig FC, Boss GR, Pilz RB (2000) Cell type-specific regulation of B-Raf
936 kinase by cAMP and 14-3-3 proteins. Journal of Biological Chemistry 275:31921-31929.

937 Robichaux WG, 3rd, Cheng X (2018) Intracellular cAMP Sensor EPAC: Physiology,
938 Pathophysiology, and Therapeutics Development. Physiol Rev 98:919-1053.

939 Schwede F, Bertinetti D, Langerijs CN, Hadders MA, Wienk H, Ellenbroek JH, de Koning EJP, Bos
940 JL, Herberg FW, Genieser H-G, Janssen RAJ, Rehmann H (2015) Structure-guided design of
941 selective Epac1 and Epac2 agonists. PLoS Biol 13:e1002038.

942 Siddiq MM, Hannila SS (2015) Looking downstream: the role of cyclic AMP-regulated genes in
943 axonal regeneration. Frontiers in molecular neuroscience 8:26.

944 Smith GM, Rutishauser U, Silver J, Miller RH (1990) Maturation of astrocytes in vitro alters the
945 extent and molecular basis of neurite outgrowth. Developmental biology 138:377-390.

946 Sofroniew MV (2009) Molecular dissection of reactive astrogliosis and glial scar formation. Trends in
947 neurosciences 32:638-647.

948 Steininger TS, Stutz H, Kerschbaum HH (2011) Beta-adrenergic stimulation suppresses phagocytosis
949 via Epac activation in murine microglial cells. Brain Res 1407:1-12.

950 Takanaga H, Yoshitake T, Hara S, Yamasaki C, Kunimoto M (2004) cAMP-induced astrocytic
951 differentiation of C6 glioma cells is mediated by autocrine interleukin-6. J Biol Chem
952 279:15441-15447.

953 Tan CL, Kwok JC, Patani R, Ffrench-Constant C, Chandran S, Fawcett JW (2011) Integrin activation
954 promotes axon growth on inhibitory chondroitin sulfate proteoglycans by enhancing integrin
955 signaling. The Journal of neuroscience : the official journal of the Society for Neuroscience
956 31:6289-6295.

957 Torres-Espin A, Santos D, Gonzalez-Perez F, del Valle J, Navarro X (2014) Neurite-J: an image-J
958 plug-in for axonal growth analysis in organotypic cultures. J Neurosci Methods 236:26-39.

959 Tucker SJ (2014) The use of fluorescence resonance energy transfer (FRET) to measure axon growth
960 and guidance-related intracellular signalling in live dorsal root ganglia neuronal growth cones.
961 Methods Mol Biol 1162:29-40.

962 Tukmachev D, Forostyak S, Koci Z, Zaviskova K, Vackova I, Vyborny K, Sandvig I, Sandvig A,
963 Medberry CJ, Badylak SF, Sykova E, Kubinova S (2016) Injectable Extracellular Matrix
964 Hydrogels as Scaffolds for Spinal Cord Injury Repair. Tissue Eng Part A 22:306-317.

965 Wang Z, Winsor K, Nienhaus C, Hess E, Blackmore MG (2017) Combined chondroitinase and KLF7
966 expression reduce net retraction of sensory and CST axons from sites of spinal injury.
967 Neurobiology of disease 99:24-35.

968 Wang Z, Dillon TJ, Pokala V, Mishra S, Labudda K, Hunter B, Stork PJ (2006) Rap1-mediated
969 activation of extracellular signal-regulated kinases by cyclic AMP is dependent on the mode of
970 Rap1 activation. Mol Cell Biol 26:2130-2145.

971 Wanner IB, Anderson MA, Song B, Levine J, Fernandez A, Gray-Thompson Z, Ao Y, Sofroniew MV
972 (2013) Glial scar borders are formed by newly proliferated, elongated astrocytes that interact to
973 corral inflammatory and fibrotic cells via STAT3-dependent mechanisms after spinal cord injury.
974 J Neurosci 33:12870-12886.

975 Wei D, Hurd C, Galleguillos D, Singh J, Fenrich KK, Webber CA, Sipione S, Fouad K (2016)
976 Inhibiting cortical protein kinase A in spinal cord injured rats enhances efficacy of rehabilitative
977 training. Experimental neurology 283:365-374.

978 Weightman AP, Pickard MR, Yang Y, Chari DM (2014) An in vitro spinal cord injury model to
979 screen neuroregenerative materials. Biomaterials 35:3756-3765.

980 Wilems TS, Sakiyama-Elbert SE (2015) Sustained dual drug delivery of anti-inhibitory molecules for
981 treatment of spinal cord injury. Journal of controlled release : official journal of the Controlled
982 Release Society 213:103-111.

983 Young W (2002) Spinal cord contusion models. Progress in brain research 137:231-255.

984 Zhou H, Li X, Wu Q, Li F, Fu Z, Liu C, Liang Z, Chu T, Wang T, Lu L, Ning G, Kong X, Feng S
985 (2015) shRNA against PTEN promotes neurite outgrowth of cortical neurons and functional
986 recovery in spinal cord contusion rats. Regenerative medicine 10:411-429.

987 Zhou M, Smith AM, Das AK, Hodson NW, Collins RF, Ulijn RV, Gough JE (2009) Self-assembled
988 peptide-based hydrogels as scaffolds for anchorage-dependent cells. Biomaterials 30:2523-2530.

989 Zhu J, Marchant RE (2011) Design properties of hydrogel tissue-engineering scaffolds. Expert review
990 of medical devices 8:607-626.

991 Zhuang Y, Xu H, Richard SA, Cao J, Li H, Shen H, Yu Z, Zhang J, Wang Z, Li X, Chen G (2019)
992 Inhibition of EPAC2 Attenuates Intracerebral Hemorrhage-Induced Secondary Brain Injury via
993 the p38/BIM/Caspase-3 Pathway. J Mol Neurosci 67:353-363.

994

995

Figure Legends

Fig. 1: The effects of Epac2 modulation on cortical neurite outgrowth. A–C, Epac2 agonist S-220 promoted significant neurite outgrowth (A, control. B, treated with S-220. C, quantification of total neurite length shows that S-220 treated neurons had significantly longer neurites). D-F, Epac2 antagonist ESI-05 significantly decreased cortical neurite outgrowth (D, control. E, treated with ESI-05. F, Quantification of total neurite length shows that ESI-05 treated neurons had significantly shorter neurites). G-I, siRNA knockdown of Epac2 significantly decreased cortical neurite outgrowth (G, scrambled siRNA control. H, Epac2 siRNA treated. I, quantification of total neurite length shows that Epac2 siRNA treated neurons had significantly shorter neurites). J-L, Overexpression of Epac protein using lentivirus promoted cortical neurite outgrowth (J, LV/GFP transduced neurons. K, LV/Epac-YFP transduced neurons. L, quantification of total neurite length shows that LV/Epac-YFP transduced neurons had significantly longer neurites). A, B, D and E cultures were grown for 24 h. G-H cultures were grown for 48 h. J-K cultures were grown for 7 days to allow enough time for gene expression. All cultures were immunostained for β-tubulin-III. Unpaired Student's t test, n = 3/group. Data expressing mean ± SEM. Scale bar: A- E, J-K: 50 μm; G-H: 100 μm.

Fig. 2: Epac agonist activates Epac protein in DRG growth cones and induces growth cone attraction. A-D, representative images of FRET SE before (A) and after (B) the addition of the Epac2 agonist S-220 and before (C) and after (D) the addition of the Epac2 antagonist ESI-05. E, FRET SE measured over time shows a significant activation and inactivation of Epac after the addition of the S-220 (blue) and ESI-05 (red), respectively, compared to control (black) (n = 4). F-G, representative images of DRG growth cones turning towards a

gradient of S-220 at time 0 (F) and 30 min (G). H, Cumulative frequency plots of turning angles show a clear switch towards the right in gradients of S-220 (blue) compared to control F12 (black), indicating greater attraction towards the direction of Epac2 activity. Average turning angles are shown above the abscissa (n = 10). Data expressing mean ± SEM. Scale bars: A-D = 10 μm; F-G = 50 μm.

Fig. 3: The Epac2 agonist overcomes inhibitory environments for cortical neuron growth. A, β-tubulin-III positive cortical neurons grew neurites on PDL coated coverslips; B, cortical neurons treated with CSPGs showed significantly shorter neurite lengths compared to control. C, Epac2 agonist S-220 attenuated the inhibitory effect of CSPGs on cortical neurite outgrowth. D, Quantification represents the percentage of change from control and shows a significant reduction in inhibition by CSPGs when S-220 was simultaneously applied. Cultures were grown for 48 h. E-G, S-220 also showed the effect in overcoming the astrocyte inhibition. Three neurite growth cone behaviors of DRG neurons co-cultured with mature astrocytes were observed: retract (∇ in E), reflect (* in E) and crossover (# in F) using time-lapse live cell microscopy. G, the quantification showed a significant reduction in the retract/reflect behaviors of neurites and a significant increase in the crossover behavior of neurites in cells treated with the Epac 2 agonist when compared to control. D, G, Mann-Whitney Rank Sum test, n = 3/group. Data expressing mean ± SEM. Scale bars, A-C = 50 μm; E-F = 25 μm.

Fig. 4: Epac2 agonist S-220 attenuates LPS induced astrocyte and microglial activation *in vitro*. Representative fluorescent images of control (A), LPS-treated (B) and LPS + S-220-treated (C) astrocytes. Representative fluorescent images of control (D), LPS-treated (E) and LPS + S-220-treated (F) microglia immunostained for Iba-1 (green) and iNOS (red). G,

Quantification of the mean fluorescence intensity of GFAP showed significant difference between control and LPS-treated astrocytes, and between LPS and LPS + S-220-treated astrocytes. H, Quantitative image analysis showing significant differences in iNOS immunoreactive cell numbers among control, LPS-treated and LPS + S-220-treated microglia. I, Greiss assay demonstrated a significant increase of nitrate concentration in the supernatant collected from LPS-treated microglial cultures when compared to that of the control. Data expressing mean ± SEM. n = 3/group. One-way ANOVA with Bonferroni post hoc test. Scale bars: 100 μm.

Fig. 5: The hydrogel degrades gradually, induces minimal immune response and supports marked neurite outgrowth in 2D cultures. A, An image of a freshly prepared gel. B, The Griess assay showed low levels of nitrite in gel culture media compared to that of LPS-exposed primary microglia cultures. C, Gel stiffness showed a gradual decrease in gain modulus from the linear region of the raw data (0 to 100 Hz, rheology). D, *In vitro* cumulative percentage drug release versus time profile. Optimization of RGD concentration to promote neurite outgrowth of DRG explants in two dimensions. E, DRG explant in gel without RGD. F, DRG explant in 1.6 mM RGD gel. G, Quantification of maximal distance of neurite outgrowth showed significant differences at 1.6 mM and 3.2 mM RGD compared to control. H, Quantification of neurite densities of DRG explants at different concentrations of RGD. I, Cortical neurons on gel without RGD. J, Cortical neurons on gel with 1.6 mM RGD. K, quantification of neurite length in gels with and without RGD, showing significantly enhanced neurite outgrowth on gels with 1.6 mM RGD. L, DRG explants grew extensive neurites in three dimensions within the gel with 1.6 mM RGD at 72 h after plating. M, Z-stack image of DRG neurons growing in three dimensions within the 1.6 mM RGD gel). N, Z plane view of DRG neurons. DRG explants were immunostained for GAP-43 (E-F). DRG

neurons and cortical neurons were immunostained for β-tubulin III (I-J, M-N). Data expressing mean ± SEM, n = 3/group. Scale bars, E-F = 200 µm; I, J and L = 100 µm; M = 50 µm. One-way ANOVA with Bonferroni's post hoc (B, D, G-H), Kruskal-Wallis ANOVA on Ranks with Tukey post hoc (C) and unpaired Student's test (K).

Fig. 6: *In vitro* evidence demonstrating the positive effects of combining the Fmoc hydrogel with Epac2 agonist application on neurite outgrowth. A-C, Assessing the effect of combining the Fmoc hydrogel with the Epac2 agonist S-220 in enhancing neurite outgrowth of DRG explants. A, Control explant growing in gel alone. B, Explant growing in gel in combination with S-220. C, Quantification of the maximal neurite length showed significantly longer neurites in the combination treatment group than the gel-only group. D-F, Assessing the effect of combining the gel with S-220 in enhancing neurite outgrowth of dissociated DRG neurons. D, DRG neurons growing in gel alone. E, DRG neurons growing in gel in combination with S-220. F, Quantification of the maximal neurite length showed significantly longer neurites in the combination treatment group than the gel-only group. Data expressing mean ± SEM. Scale bars, A = 250 µm; B = 500 µm; D-E = 100 µm. Unpaired Student's *t* test, n = 3/group.

Fig. 7: Timeline, study design and schematic diagram of *ex vivo* preparation on organotypic spinal cord culture. A, Timeline of the experiments. B, Schematic diagram depicting the production and lesioning of organotypic spinal cord slice cultures. C, Quantification of live/dead assay did not show any difference before and after lesion (n = 10-15/group). D, Representative lived/dead-stained fluorescence micrograph of a slice before lesioning and 2 days post-lesion. E-I, Using the *ex vivo* model we found that, at 7 days post-injury, treatment with either S-220 or hydrogel alone produced similar degrees of neurite outgrowth into the

lesion gaps, but significantly more than that of the non-treated slices (E, non-treated slice; F, S-220- treated slice; H, hydrogel treated slice; I, combination treated slice; white dashed lines indicate lesion margins). The agonist was added to culture media. G, The axonal profile analysis showed that, when the gel was combined with S-220, there was significantly more axon growth in the lesion gap than those following treatments with S-220 or hydrogel alone. C, Data expressing mean ± SEM. G, Data expressing mean ± SEM (box limits), bars above and below each box = 5% & 95% confidence limits. Circles represent individual biological replicates (n = 4 - 6). One-way ANOVA, Bonferroni's post hoc test. Scale bars, D = 500 μm; E-I = 200 μm.

Fig. 8: S-220 incorporated into the hydrogel promotes neurite outgrowth and suppresses astrocyte activation. A-B, Representative images showing significant difference in neurite outgrowth between gel only (A) and gel + 5μM S-220 (B). White dashed lines indicate lesion margins. C, Neurite growth profiles across the lesion gap, showing a progressive increase with gel only and gel + 5 μM S-220. D, Quantification showing the numbers of β-tubulin III^+ processes per mm^2 between control and different concentrations of S-220 delivered in the gel, with 5μM having the greatest effect. E-G, Representative images exhibit astrocyte activation in the lesion using GFAP staining as an astrocyte marker. E, Control. F, Gel only. G, Gel + 5μM S-220. H, Quantification of the GFAP immunoreactivity intensity showed a significant reduction of mean grey value (OD) in gel + 5μM S-220 compared to the control and the gel only treatment. I, Representative image of the relationship between GFAP (red) and β-tubulin-III (green) immunoreactive processes in a control injury condition. J, Higher magnification image showing the collapse of growth cones (white arrowheads) when they meet activated astrocytes. K, Representative image of the relationship between GFAP and β-tubulin-III immunoreactive processes in a lesion with combined treatment with gel + 5 μM S-

220. M, Higher magnification image showing the alignment of the astrocytes and β-tubulin-III immunoreactive processes (white arrowheads). N-O, Levels of astrocyte reactivity were estimated by the overlapping of GFAP (red) and nestin (green). N, Representative image of GFAP/nestin reactivity in lesion sites of non-treated slices. O, Representative image of GFAP/nestin overlapping in slices treated with S-220 delivered by the hydrogel. P, Quantification of GFAP/nestin pixel overlapping. Data in D, H and P are expressed as mean ± SEM (box limits). Bars above and below each box = 5% & 95% confidence limits. Circles represent individual biological replicates (n = 4-6). One-way ANOVA with Bonferroni's post hoc test. Scale bars, A-B, E-G and N-O = 100 µm; I, K = 50 µm; J, M = 25 µm.

Fig. 9: S-220 incorporated into the gel suppresses microglia activation in lesioned spinal cord slice. A, Iba-1 immunoreactive cells inside the injury site in control lesion slices (white asterisks, indicating activated morphology). B, Iba-1 immunoreactive cells inside the injury site in combination treated slices (yellow arrowheads, indication resting morphology). C, Non-injured microglia (yellow arrowheads, indicating resting morphology). D, Cell body perimeter was quantified and used as an indication of activation. Cell body size decreased more significantly in the presence of the hydrogel only or hydrogel + 5 µM S-220, respectively. E, Representative image of the relationship between GFAP and Iba-1 immunoreactive cells in an injured control. F, Representative image of the relationship between GFAP and Iba-1 immunoreactive cells in injured slices treated with a combination of hydrogel + 5 µM S-220. Data in D are expressed as mean ± SEM (box limits). Bars above and below each box = 5% & 95% confidence limits. Circles represent individual biological replicates (n = 4). One-way ANOVA with Bonferroni's post hoc test. Scale bars, A-C = 25 µm; E-F = 50 µm.

Fig. 10: S-220 delivered by Fmoc hydrogel into the lesion of contusion injured spinal cord enhances locomotor functional recovery. Both S-220-treated and non-treated contusion-injured animals showed similar levels of locomotor function at 3 weeks post-injury as assessed on the BBB open field task. However, by 2 weeks after treatment (indicated by the black arrow), S-220-treated animals showed significantly better locomotor function (3 points on the BBB scale) compared with the non-treated animals, a difference was maintained until 4 weeks after treatment (the last time point assessed). Data were analyzed with two-way ANOVA followed by Bonferroni's *post hoc* test. n = 4-5. Data were expressed as mean ± SEM. * $p < 0.05$.

Fig. 11: A schematic diagram summarizing the potential mechanisms of Epac2 activation by S-220 in the *in vitro* and *ex vivo* studies. The blue dotted rectangle and blue dotted arrows summarizes the mechanisms for *in vitro* studies. The red dotted rectangle and red dotted arrows summarizes the mechanisms for *ex vivo* studies. Our findings from the *in vitro studies* with individual monocultures of neurons, astrocytes, and microglia demonstrate that S-220 has direct and individual effects on: (a) neurons, promoting their growth possibly via the subsequent activation of Rap-1/B-Raf/ERK signaling pathway (Murray and Shewan, 2008; Murray et al., 2009; Wei et al., 2016); (b) astrocytes, reducing their activation by LPS possibly via IL-6/STAT3 signaling pathway (Takanaga et al., 2004); and (c) microglia, reducing their activation by LPS possibly via arginase I signaling pathway (Ghosh et al., 2016). S-220 binds to the cyclic nucleotide binding (CNB) domains of Epac2 protein within these cells triggering downstream signaling pathways (Tucker, 2014). Our findings from the *ex vivo studies*, however, suggest that S-220 manifests its effects on these cells in a more complex and intermingled manner: (1) elongated astrocytes following S-220 treatment may resemble radial glial progenitors, releasing axon-growth supporting molecules (Garcia et al.,

2004); (2) elongated astrocytes following S-220 treatment may provide direct guidance for axonal growth (Anderson et al., 2016); (Robichaux and Cheng) reduced astrocyte activation by S-220 may lead to upregulate the gene for NMDA receptor subunit NR2C, which is a key part in the tripartite synapse regulating astrocyte-neuron communication (Paco et al., 2016); (4) reduced astrocyte activation by S-220 may down-regulate the genes responsible for the production of proteoglycans including CSPGs, thereby reducing their inhibitory effects on axonal outgrowth (Paco et al., 2016); (5) reduced astrocyte activation by S-220 may involve STAT-3/nestin, and subsequently may regulate other inflammatory cell behavior, such as that of microglia at the spinal cord lesion site (Wanner et al., 2013); and (6) reduced microglial activation via astrocyte regulation may lead to reduced production of proinflammatory mediators (Steininger et al., 2011), thereby promoting axonal outgrowth. It is also highly likely that S-220 may have direct and individual effects on these three types of cells in the *ex vivo* model, including transcriptional changes in arginase I, interleukin-6, secretory leukocyte protease inhibitor, and metallothionein in neurons (d) (Hannila and Filbin, 2008; Siddiq and Hannila, 2015), which have been shown to promote axonal outgrowth and overcome inhibitory molecules. Red and blue small circles with diagonal across = stop/inhibit.

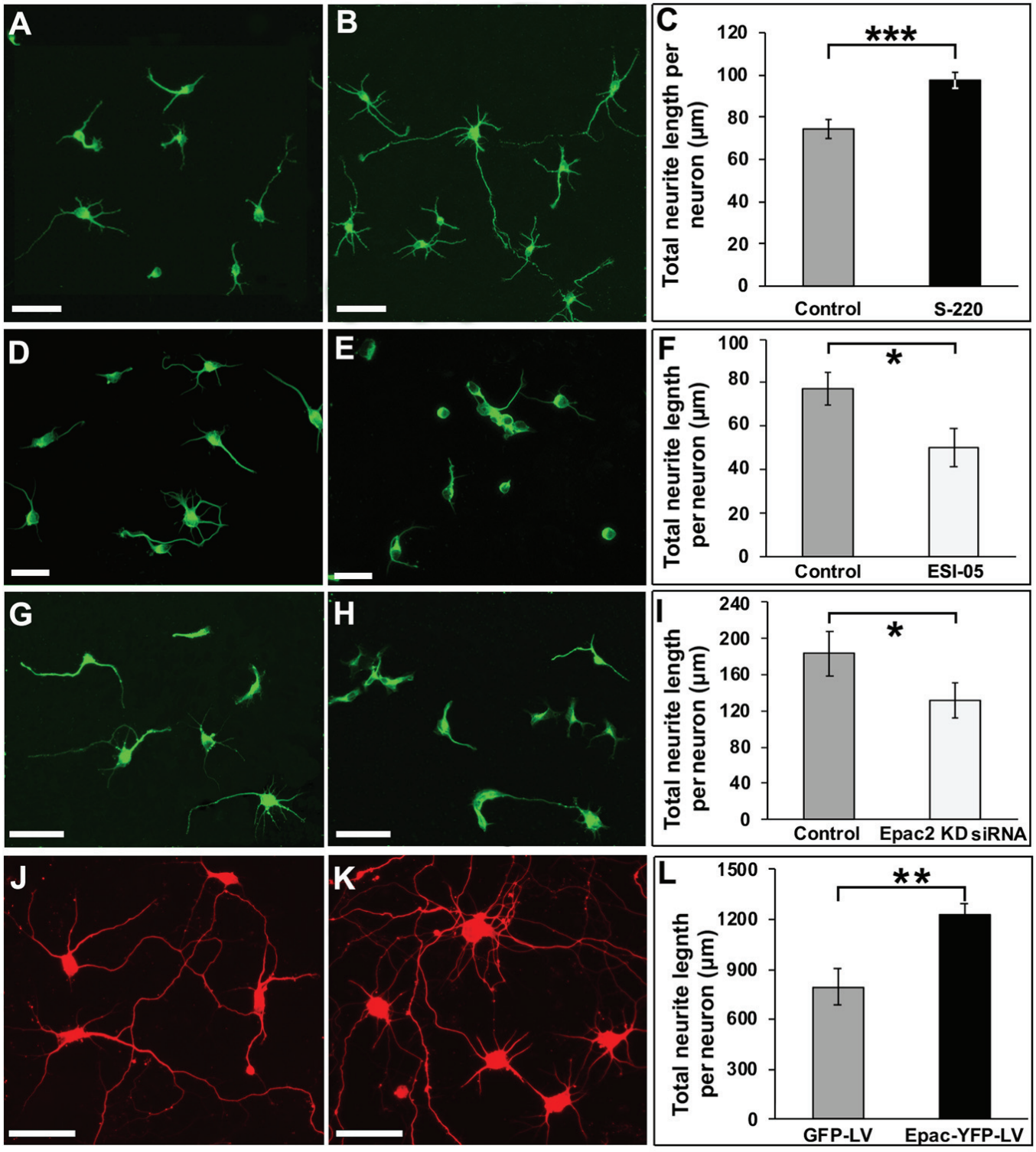

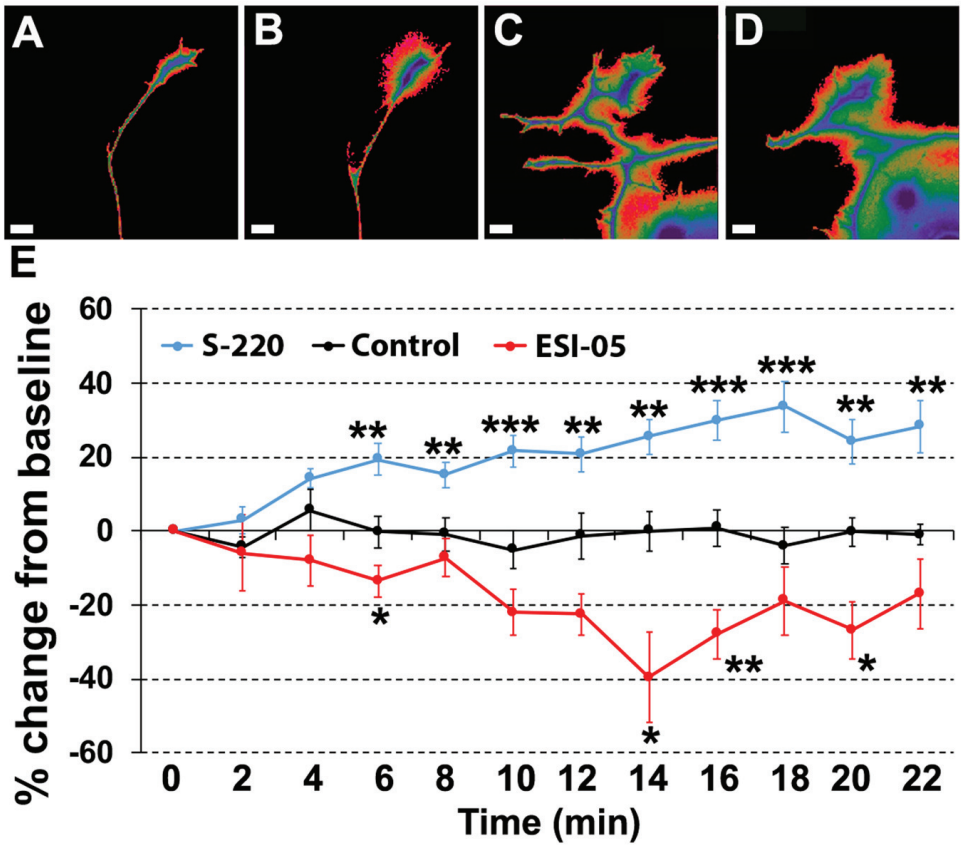

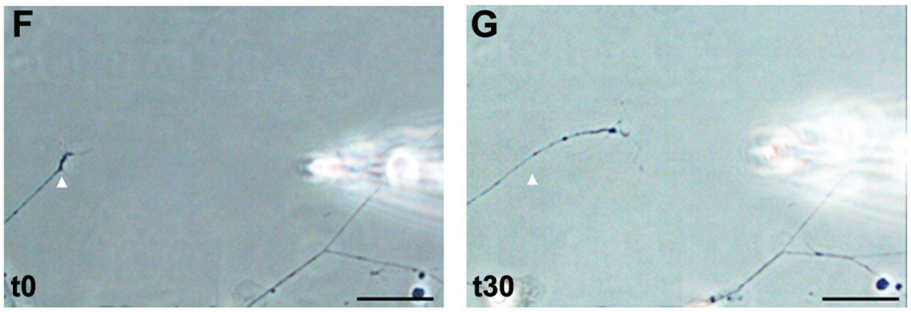

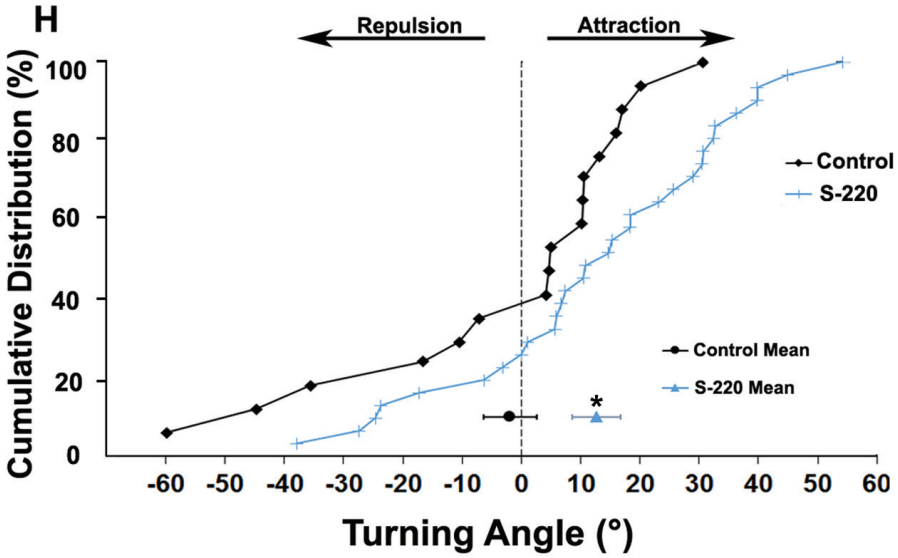

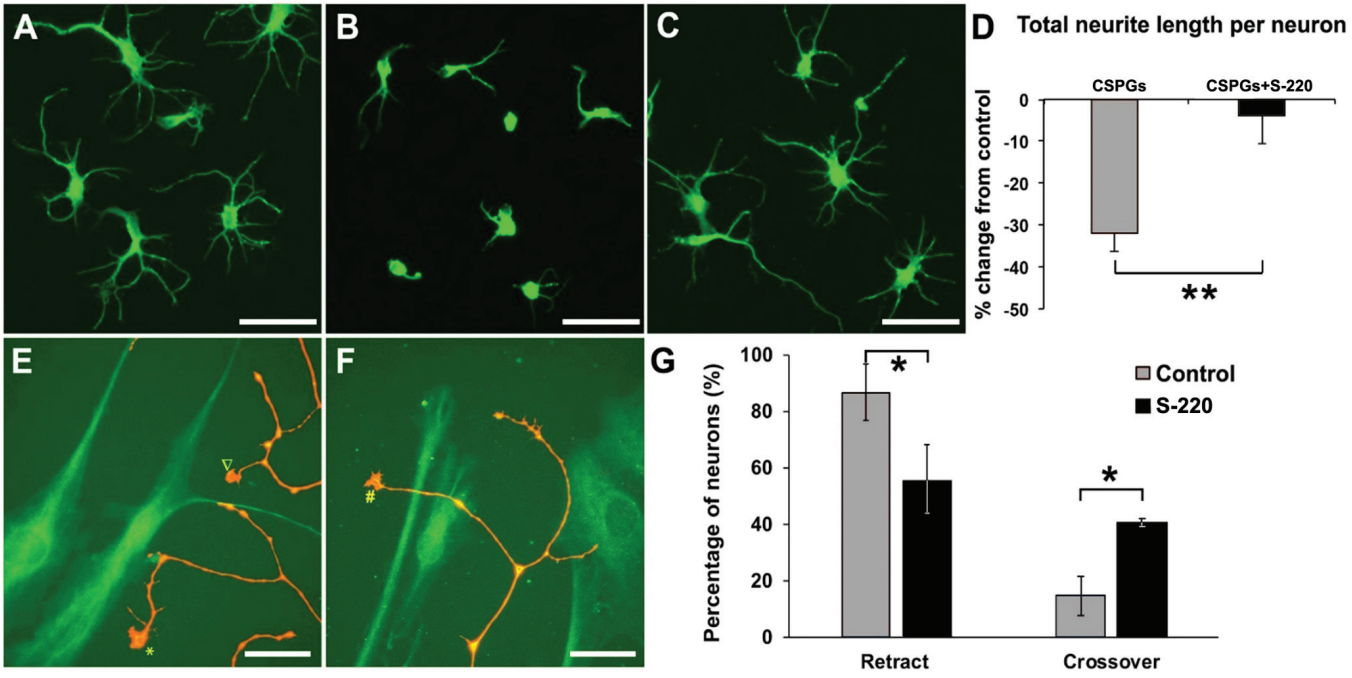

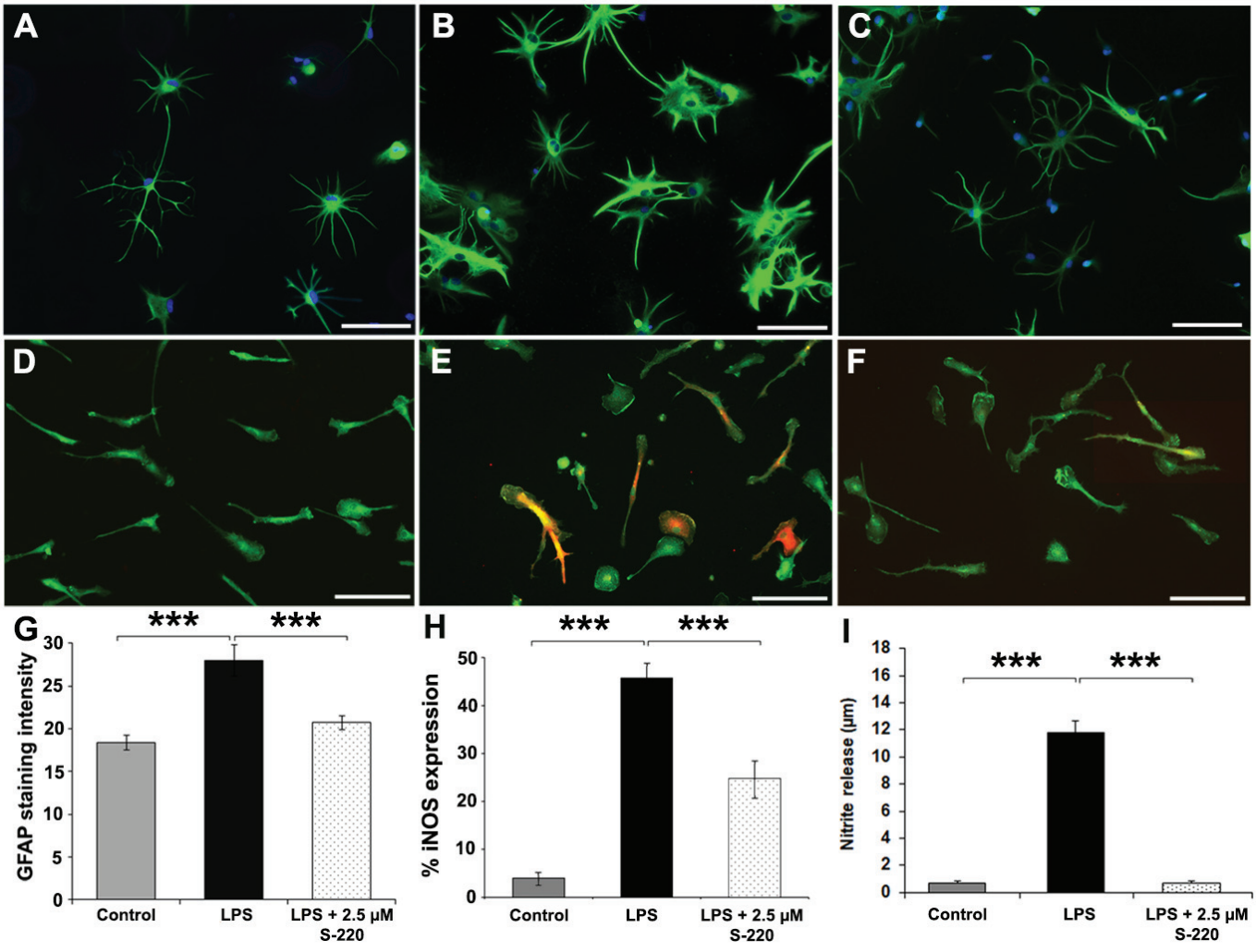

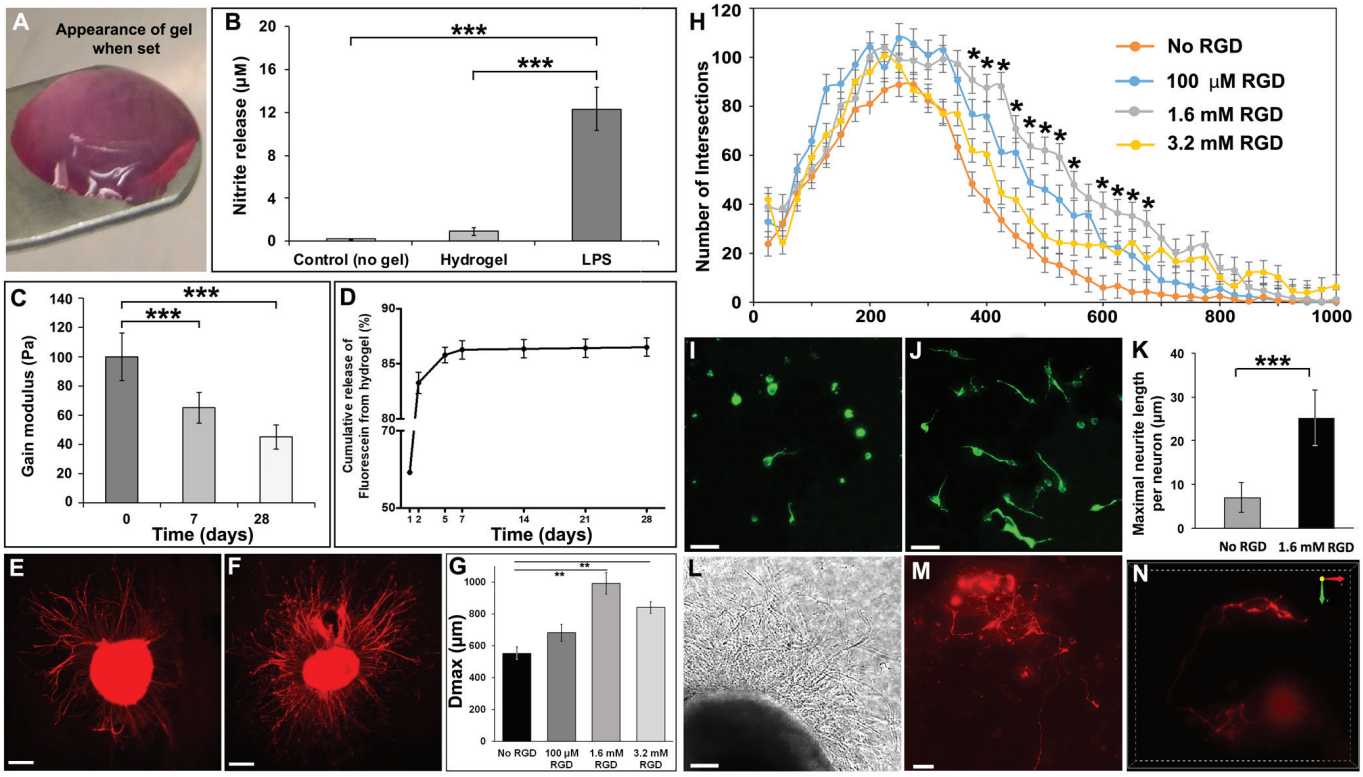

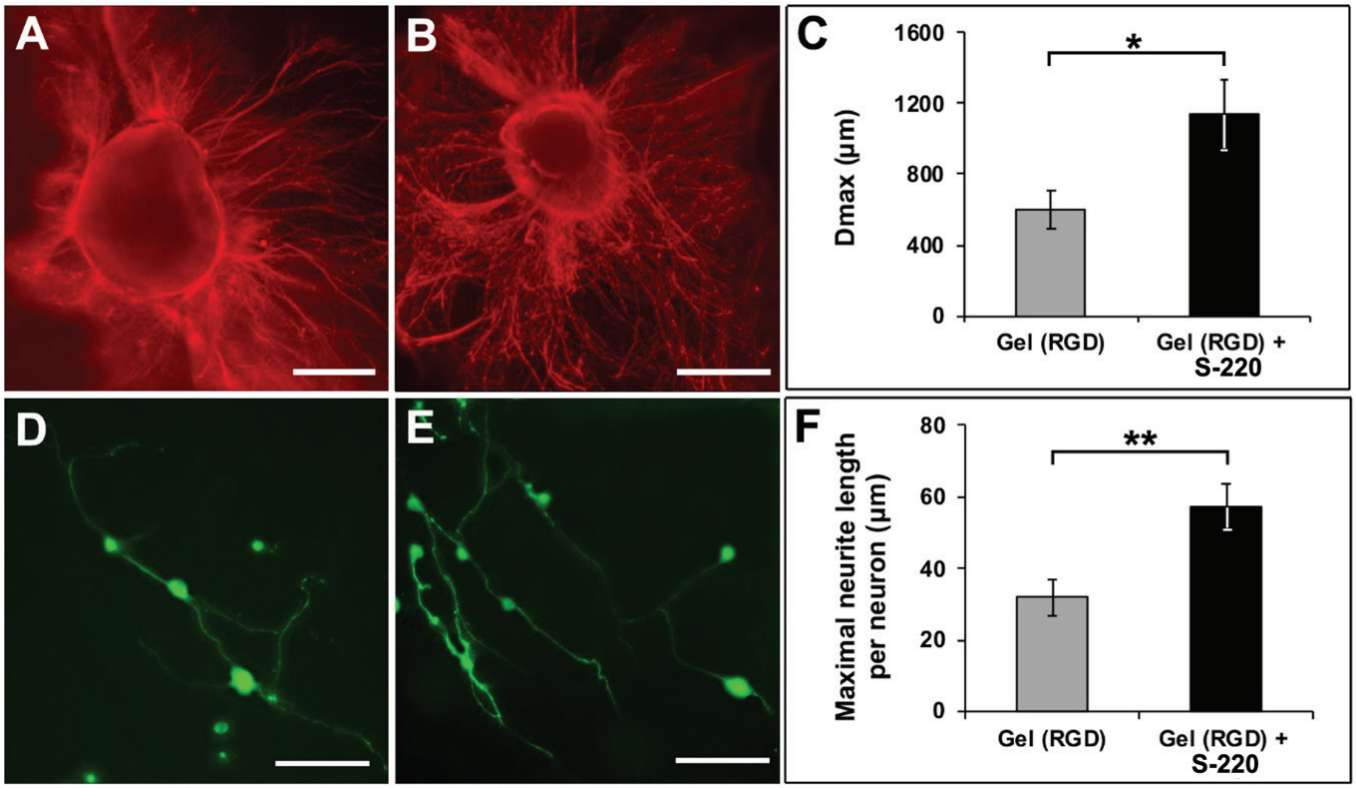

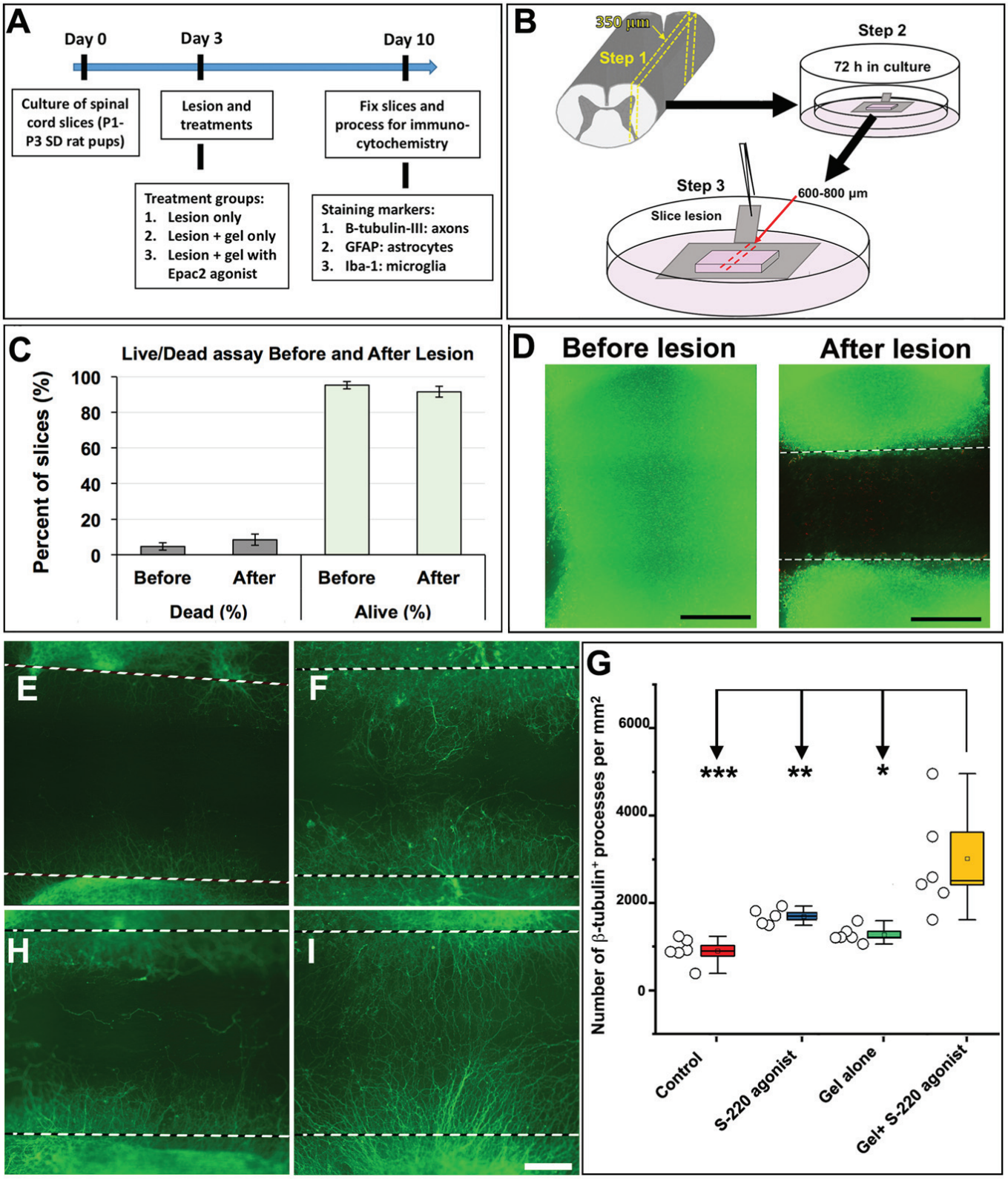

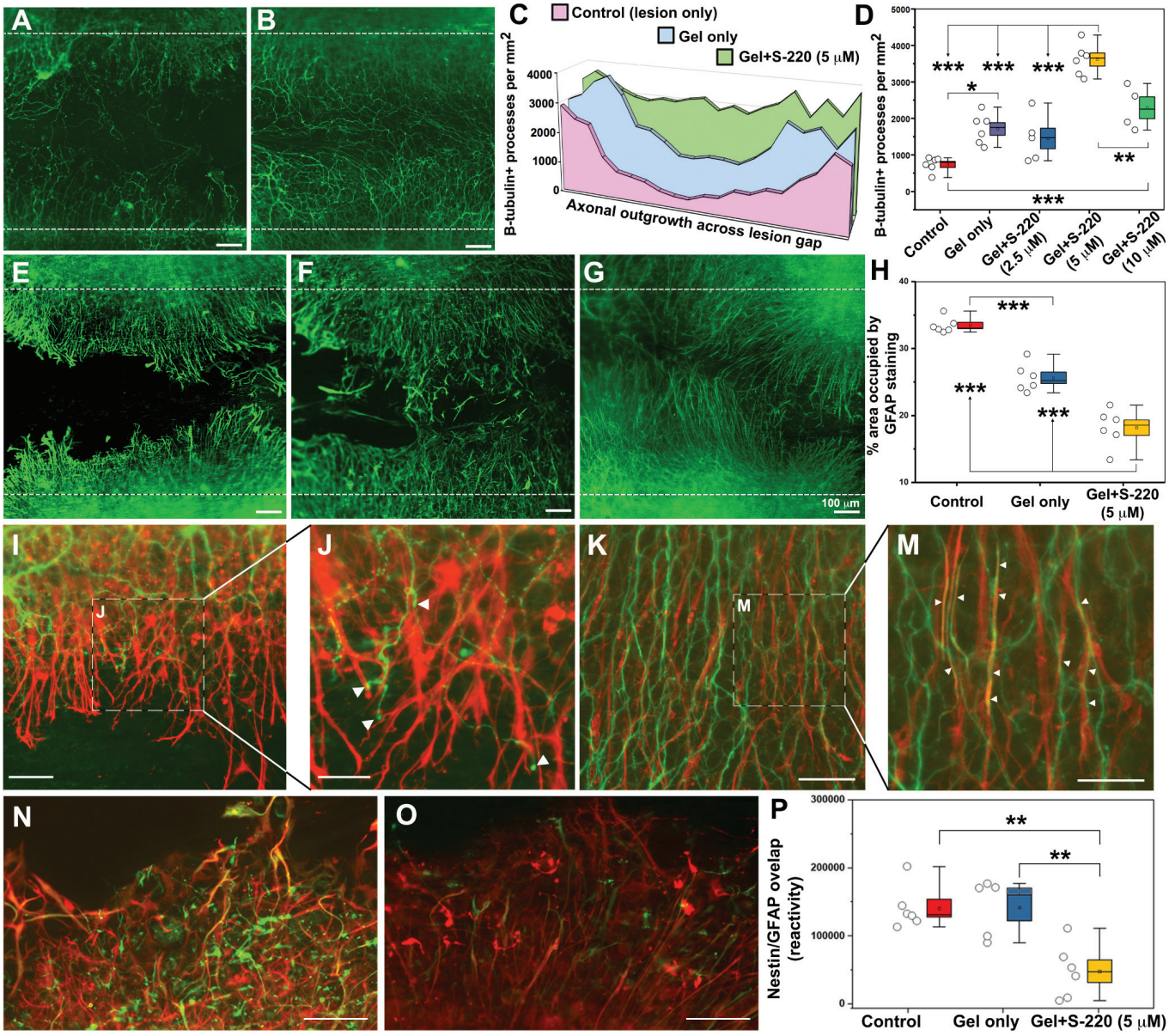

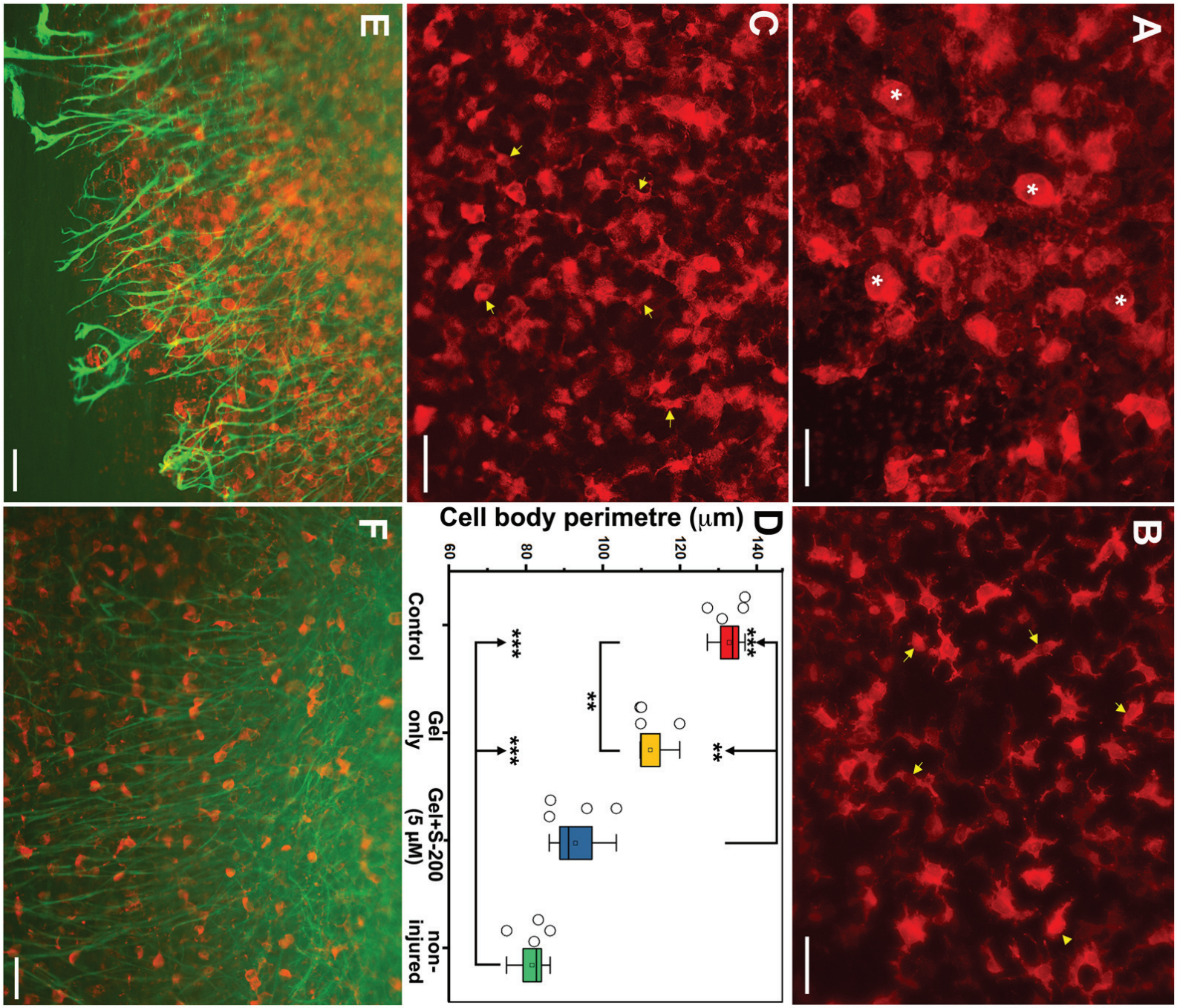
A
B
C
D
E
F
Cell body perimetre (μm)
60
80
100
120
140
Control
Gel only
Gel+S-200 (5 μM)
non-injured
***
**
**
***
***